ChemElectroChem

Review
doi.org/10.1002/celc.202300761

Chemistry Europe
European Chemical Societies Publishing

www.chemelectrochem.org

Alkali Containing Layered Metal Oxides as Catalysts for the Oxygen Evolution Reaction

Mario Falsaperna,*[a] Rosa Arrigo,[b] Frank Marken,[a] and Simon J. Freakley*[a]

Improving the efficiency of the oxygen evolution reaction (OER) is essential to realise energy systems based on water electrolysis. Many catalysts have been developed for the OER to date, with iridium-based oxides being the most promising due to their relative stability towards corrosion in acidic electrolytes under oxidising potentials. In recent years, examples of catalysts adopting layered structures have been shown to have promising characteristics such as higher conductivity and higher electrochemically active surface area compared to highly crystalline metal oxides. Furthermore, such materials possess additional tuneable properties such as interlayer spacing, identity and concentration of the interlayer species, edge and interlayer active sites, and higher active surface area. Recent attention has focused on mono- and polymetallic lithium-containing layered materials, where the presence of interlayer lithium cations, *in situ* delithiation processes and combinations of transition metal oxides result in enhanced catalytic properties towards OER. This review aims to provide a summary of the recent developments of such layered materials, in which lithium or other alkali metal ions occupy interlayer sites in oxides.

1. Introduction

The combustion of fossil fuels is still our most abundant energy source, but also the main source of CO_2 emissions in the transportation and manufacturing sectors. A societal shift to renewable energy is required to underpin global sustainability targets where the efficient storage of renewable energy in chemical bonds is crucial for carbon neutrality. Hydrogen has a high specific energy density (~142 MJ kg^{-1}) and is an attractive target to store intermittent renewable energy.[1] However more than 90% of hydrogen is currently produced from fossil fuel resources through steam methane reforming rather than water electrolysis.[2,3] The balance between which technology is preferred is determined in part by the relative costs of natural gas *vs* electricity and, while efficient carbon capture can reduce the kg_{CO_2}/kg_{H_2} of methane steam reforming, projections of decreasing renewable energy costs will eventually remove the need for fossil fuels as a feedstock for H_2 production.[4]

Water splitting is a key technology for green H_2 production, consisting of two half-cell reactions, the hydrogen evolution reaction (HER) and the oxygen evolution reaction (OER) (see Figure 1). While the HER proceeds efficiently over Pd and Pt catalysts with minimal energetic barriers, the OER severely limits overall reaction rates due to the slower kinetics of this $4e^-$
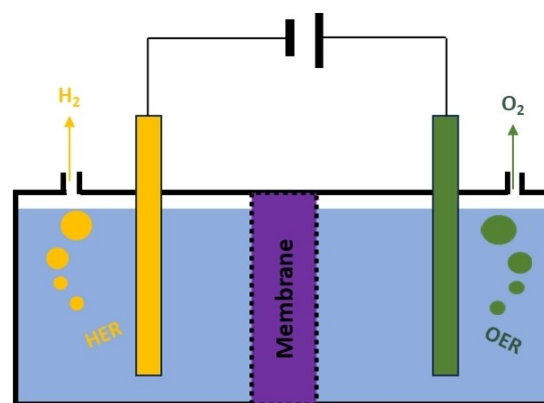
Figure 1. Schematic diagram of a water splitting electrochemical cell showing the two half-reaction cells for the HER and the OER separated by a membrane.

transfer reaction. State-of-the-art iridium oxide electrocatalysts require an additional 0.3–0.6 V of overpotential (η) above the thermodynamically required potential (1.23 V$_{RHE}$) at standard conditions to overcome activation barriers of rate-determining steps.[5] A challenge to the adoption of large-scale electrolysis is to therefore design new catalysts that decrease the overpotential needed for the OER and are ideally able to operate over a wide pH range, with high current densities, and stability over an extended periods.

Transition metal compounds, such as Co-, Ni-, Fe-, and Mn-based oxides/hydroxides were found to catalyse the OER more than half a century ago[6–11] and have attracted significant interest due to their low material cost, easily mediated structure, and high OER activity, making them promising catalysts to replace noble metal oxides. However, these materials often suffer from poor stability due to corrosion under harsh acidic and anodic conditions over extended periods of time. A greater understanding of the fundamental material properties dictating the water electrolysis process is needed to

[a] M. Falsaperna, F. Marken, S. J. Freakley
     Department of Chemistry, University of Bath, Claverton Down, Bath, BA2 7AY, UK
     E-mail: mf975@bath.ac.uk
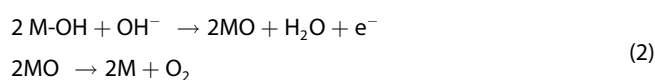   s.freakley@bath.ac.uk

[b] R. Arrigo
   School of Science, Engineering and Environment, University of Salford, M5 4WT Manchester, UK

design more resistant and efficient electrode materials for the OER.

1.1. Mechanistic Considerations

Descriptors for fundamental reaction steps have been derived from theoretical analysis of the OER mechanism and can be used to describe the structure-activity relationship of catalysts in terms of activity. The OER can be regarded as four proton–electron-transfer steps involving several intermediates at the catalyst surface. Earlier mechanistic proposals in alkaline conditions include for example Bockris's oxide pathway (equation (1)) or the electrochemical oxide path (equation ((2)), in which the initial oxidation of the metal surface leads to adsorbed hydroxide, followed by a proton transfer (1) or electron-proton coupled transfer (2) that forms the M—O species. These further react by recombination or nucleophilic attack from solvent molecules (associative mechanism) forming various metastable reaction intermediates (*e.g.* peroxide, superoxide) eventually leading to the evolution of oxygen which regenerates the catalytic site.

$$M + OH^- \rightarrow M\text{-}OH + e^-$$
$$2\,M\text{-}OH \rightarrow MO + M + H_2O \tag{1}$$

$$2\,M\text{-}OH + OH^- \rightarrow 2MO + H_2O + e^-$$
$$2MO \rightarrow 2M + O_2 \tag{2}$$

These peroxide and superoxide species are explicitly included in the mechanism suggested by Kobussen.

$$MO + OH^- \rightarrow MO_2H^-$$

$$MO_2H^- + OH^- \rightarrow MO_2^- + H_2O + e^-$$
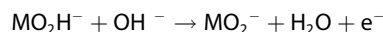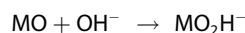
The enthalpy of lower to higher oxide transition and the surface oxygen binding energy have been proven to be descriptors of the electrocatalytic performance of different metal oxides following the Sabatier principle.[12] This supports the idea that the active phase during the OER is an oxide phase,[12–14] and therefore mechanistic studies have mainly focused on oxide surfaces.[15] The theoretical description developed by Rossmeisl *et al.* considers the overall reaction rate depending on the free energy of the potential determining reaction step (PDS) involving catalyst-bound intermediates.[15] Using this approach, the properties of single crystal rutile type oxide surfaces were examined, namely RuO_2, IrO_2, and TiO_2, and the lower O_2-evolving potentials of RuO_2 and IrO_2 can be attributed to weak oxygen (O_2) binding and strong hydroxyl binding on their surfaces. The nature of the PDS depends on the strength of oxygen binding at each surface: for strongly bound oxygen species, O-OH formation is the PDS that forms bonds between surface M—O and OH^-; for weakly bound oxygen, the formation of M—O is typically the PDS.

The approach of evaluating the adsorption energy of various intermediates M—O, MOH, MOOH to determine the PDS

Dr. Simon Freakley completed his MChem at Durham University in 2009 and PhD in 2012 under the supervision of Prof. Graham Hutchings at the Cardiff Catalysis Institute focused on the direct synthesis of hydrogen peroxide. Following this Simon remained at the CCI working on projects including methane oxidation and acetylene hydrochlorination. In 2018 Simon moved to the University of Bath as a Prize Research Fellow in Sustainable Technology and was appointed to a Lectureship in 2021. His current research interests include metal oxide catalysts for OER, hydrogenation and dehydrogenation reactions, and integration of plasmonic nanoparticles into catalysis.

Dr. Mario Falsaperna obtained his MSc in Materials Chemistry in 2018 from the University of Catania, Italy, working on MOFs for gas separation. He obtained his PhD in Chemistry from the University of Kent, UK, working on coordination polymers exhibiting magnetocaloric properties and their optimisation for low-temperature magnetic refrigeration, with an interest in their frustrated and low-dimensional magnetic states. In 2022, he joined the Department of Chemistry at the University of Bath as a postdoctoral associate. His work focuses on the development, characterisation and testing of novel alkali metal-containing iridium-based catalysts for water electrolysers.

Prof. Frank Marken obtained a Dr. rer. nat. degree at RWTH Aachen (Germany) and was Feodor-Lynen Fellow at La Trobe University, Melbourne (Australia). He worked as Stipendiary Lecturer at Oxford and at Loughborough University (UK). In 2004 he moved to the University of Bath. In 2011 he was promoted to a personal chair in physical chemistry. Research is linked to the Institute of Sustainability (IoS) and the Water Innovation Research Centre (WIRC) at Bath and focused on pure and materials electrochemistry, photoelectrochemistry, electroorganic processes, and new types of membrane processes for water purification and desalination.

Dr. Rosa Arrigo is Associate Professor in Inorganic Chemistry at Salford University and honorary scientist at Diamond Light Source. She obtained a MSc in Industrial Chemistry at the University of Messina, and PhD in Natural Science at TU Berlin. Following a FHI-postdoctoral fellowship, she was group leader at MPI-CEC, contributing pioneering work on interfacial spectroscopy for electrocatalysis. Her research is concerned with the design of catalytic/electrocatalytic materials for sustainable chemistry and energy, aided by the application of operando spectroscopic techniques. She is elected member of the RSC-Dalton-Community, and acts as the chair of the PRP of the ESRF Xmas beamline.

ChemElectroChem

Review
doi.org/10.1002/celc.202300761

Chemistry Europe
European Chemical
Societies Publishing

provides a transferable approach which can explain reactivity trends amongst various oxides. Based on the development of a universal scaling relationship, theoretical overpotentials can be predicted for a range of oxide surfaces using $\Delta G_{O^*}-\Delta G_{HO^*}$ as a descriptor for the oxygen evolution activity supported by many experimental studies. For Ir, Ru and Pt oxides with rutile structures, Mn oxides and Co oxides, the activity suggested by the theoretical calculations follows: $Co_3O_4 \approx RuO_2 > PtO_2$ rutile $\approx RhO_2 > IrO_2 \approx PtO_2$ β-phase $\approx Mn_xO_y$. The conclusions of these studies demonstrated that for this class of materials, the OER activity could not be significantly improved beyond RuO_2 by tuning the binding between the intermediates and the catalyst surface. However, the observation of scaling relationships between descriptors used to explain the OER over planar crystalline surfaces might overly restrict design possibilities. For example, the thermochemical analysis neglects the influence of water molecules, and the hydrogen bonding networks that surrounding the intermediate species. As such, it is possible that three dimensional structures, rough surfaces or co-adsorbates on the surface could achieve a greater relative stabilization of HOO*.

In the development of new OER catalysts, the objective is now to understand the factors governing catalytic activity well enough to design catalysts from the bottom up in a way that breaks these scaling relationships. Additional activity descriptors are essential to capture the complexity of high surface area or poorly ordered electrocatalysts. Strategies to break linear scaling relationships are aimed at the stabilization of HOO* *via* proton acceptor functionality or switching the OER pathway towards the involvement of lattice in addition to surface oxygen.[16,17]

The question as to whether the lattice-oxygen-mediated mechanism (LOM), or rather the chemisorbed oxygen adsorbate evolution mechanism (AEM) takes part in the OER is still subject to debate (see Figure 2). The activity and stability of metal oxides can depend strongly on the predominant mechanism of the OER that is occurring at the surface – either O_2 formation involving surface/subsurface oxygen from the oxide or O_2 formation purely from adsorbed H_2O molecules.[18] The associative or recombination mechanism would necessarily lead to the generation of a vacancy. In other mechanisms involving the nucleophilic attack of water molecules with adsorbed OH⁻ species, the process is constricted to surface species without the generation of an oxygen vacancy. Isotopic labelling experiments aiming to clarify the involvement of the surface oxide layer under anodic polarization appear show that O exchange between the solvent and rutile IrO_2 surface occurs rapidly under OER conditions.[19] The generation of vacancies tends to make the electrocatalysts more prone to solvation and corrosion which can lead to solvated metal-oxo species which are highly oxidising and capable of liberating O_2 from H_2O oxidation before re-deposition on to the catalyst surface.[20,21] Tafel slopes can provide a relevant indication of reaction kinetics through the determination of the dependence of increasing voltage on measured current. Hence, low values of Tafel slopes are indicative of faster kinetics. Low Tafel slopes are typically reported for Ru and Au materials, however these materials tend to show relatively high dissolution rates, suggesting a predominant LOM mechanism with significant vacancy formation. In contrast, for materials showing high Tafel slopes such as Pd/Pt an AEM mechanism is characterized by low dissolution rates.[22]

1.2. Iridium and Ruthenium Oxides

Iridium oxides realize a compromise between moderate Tafel slopes and steady-state stability, with the lower onset potential for oxygen evolution and highest corrosion resistance. The
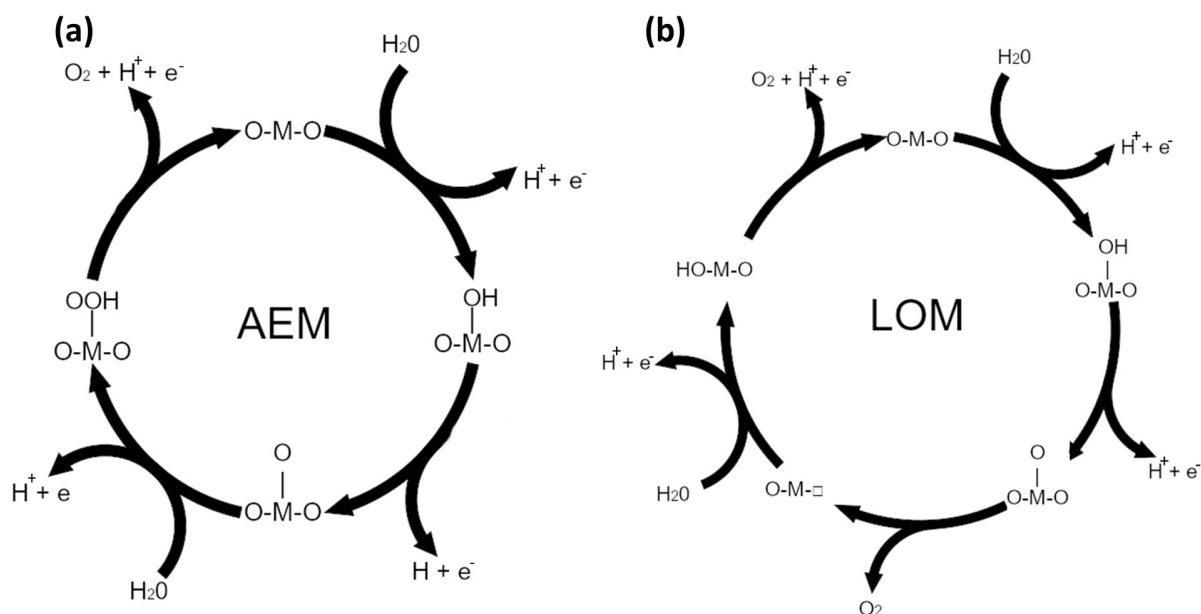
Figure 2. Catalytic cycles of the (a) absorbate evolution mechanism (AEM) and (b) the lattice-oxygen-mediated mechanism (LOM).

evidence of both types of mechanisms occurring simultaneously on IrO_2 has led to the postulation that this characteristic is at the origin of its unmatched OER performances.[22] Consequently, electrocatalysts such as iridium (IV) oxide (IrO_2) adopting a rutile structure of corner-sharing octahedral [MO_6] units (see Figure 3a), is regarded as being the benchmark catalysts for OER in acidic electrolytes. The crystallinity of the material has a strong influence on the catalytic activity and stability, as shown by the contrast between crystalline and amorphous IrO_2 (see Figure 3b). The latter features a significantly higher activity but lower stability when compared to rutile IrO_2, which, in contrast, shows relatively lower activity but higher stability.[23]

Rutile RuO_2 (r-RuO_2) is severely limited by low stability compared to r-IrO_2, particularly in acidic media in combination with anodic potentials which leads to fast corrosion *via* the formation of volatile RuO_4 which undergoes hydrolysis in the electrolyte to precipitate RuO_2.[24]

Approaches to probe the mechanism of the OER have focused on the surface electronic structure properties that are proportional to the binding energies of oxygen at the metal and oxide surfaces, including d-band centre,[14] and p-band centre,[26] and metal–oxygen hybridization. *operando* studies of structural properties can provide experimental evidence and activity descriptors to establish relationships between performance and structural dynamics towards mechanistic insights into the oxygen turnover as well as the degradation mechanism. Techniques such as X-ray absorption spectroscopy (XAS), X-ray photoemission spectroscopy (XPS) and X-ray diffraction (XRD), as well as infrared (IR) and Raman spectroscopy have been successfully applied in *operando* to study polarised liquid/solid interfaces. XAS in the hard X-ray regime (energy higher than 10 kV) is extensively applied to study electrocatalysis due to the high penetration depth of the X-rays meaning minimal adaption of reaction cells is required. O K-edge soft X-ray *operando* studies were used to monitor oxygen species during OER over Ir oxide systems and led to the identification of non-innocent (redox active) oxyl ligands *via* potential-dependent

OH deprotonation. The electrophilic character of the oxyl group is postulated to lead to the O–O bond formation by nucleophilic attack of water in the chemical rate determining step.[27] By means of XPS analysis, the formation of electron-deficient terminal or bridged O species is associated with the generation of Ir with oxidation state $> +5$.[28,29] This is consistent with bulk electronic structure analysis.[30] where it was found that amorphization of the oxide, as seen by the increase of the Ir L edge NEXAFS,[31] leads to enhanced performance at the expense of stability against dissolution.[20] An amorphous material while more flexible can undergo more rapid O-coupling reactions than a highly stable crystalline material but is more susceptible to degradation due to the isotropic character of the metal-oxygen bonds. In many cases, the activity and stability of IrO_2 oxides are inversely correlated.

Recently, it has been shown the synthesising amorphous iridium oxyhydroxides through simple hydrothermal methods in the presence of various alkali metal salts can modulate the activity and stability of the materials. The difference in activity has been ascribed to a number of factors, including the structural flexibility offered by the amorphous structure, the morphology and size of the particles and the simultaneous presence of mixed Ir(III)/Ir(IV) species.[32] Among these electrocatalysts, those synthesised using LiOH or Li_2CO_3 show promising activity compared to commercially available IrO_x and r-IrO_2. In particular, the catalyst synthesised using Li_2CO_3 exhibits the highest activity among its analogues with an overpotential of 250 mV at 22 mA cm^{-2} and improved stability by an order of magnitude at 10 mA cm^{-2} compared to commercially available IrO_x. Subsequently, further development of alkali metal-doped iridium oxides suggests that key structural features allow the inverse relationship between stability and activity to be broken. On thermal treatment the residual Li^+ suppresses rutile IrO_2 formation which commonly deactivates amorphous iridium oxyhydroxides and instead drives the formation of a layered material with interstitial alkali metal cations[28] Similarly, Fe substitution into inactive cobalt oxide spinels has been shown to enable an *in-situ* transformation into active oxyhydroxide
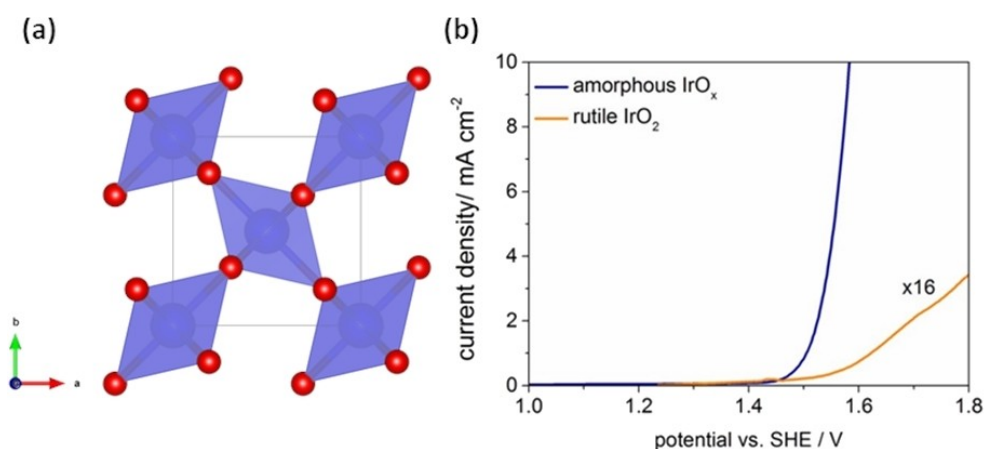
Figure 3. (a) View of the unit cell of the rutile IrO_2 crystal structure along the *c*-axis, showing the corner-sharing [IrO_6] octahedra and (b) LSV of commercially available r-IrO_2 (Sigma Aldrich) and amorphous IrO_x powders (Alfa Aesar) at 5 mV s^{-1} in 0.5 M H_2SO_4, with current density of r-IrO_2 x16 to normalise geometric surface area. Adapted from ref.[25] with permission from the PCCP Owner Societies.

ChemElectroChem

Review
doi.org/10.1002/celc.202300761

**Chemistry Europe**
European Chemical
Societies Publishing

electrocatalysts. During polarisation the material showed a transformation into a layered structure with enhanced structural flexibility as well as a much shorter distance between O species in the interlayer space, leading to both surface oxygen vacancies and lattice oxygen involvement in the reaction.[33–35] Recently, due to the costs of Ir and Ru here has been a significant focus on Ni-based oxides and hydroxides, including $Ni(OH)_2$ and doped NiOOH. Studies have shown lithium can have a significant doping effect on catalyst activity, by changing the local electronic structure of nickel, improving OER activity.[36,37]

1.3. Layered Materials as Electrocatalysts for the Oxygen Evolution Reaction

Materials which feature high populations of exposed active sites are desirable as electrocatalysts. Layered materials are particularly suited for this purpose due to their tuneable interlayer spacing and species, high populations of edge and surface sites and high ion mobility. Layered double hydroxides (LDHs) have attracted significant due to their promising performance towards the OER.[38] LDHs have a general formula $M^{2+}_{1-x}M^{3+}_x(OH)_2(A^{n-})_{x/n} \cdot yH_2O$, where M is divalent and trivalent transition metal cations and A^{n-} are interlayer anionic species (see Figure 4a). LDHs offer widely tuneable compositions and synthetic routes, therefore enabling flexible electronic structures, morphologies and physicochemical properties.[38] Wu *et al.* have recently shown how a binary LDH, NiFe-LDH, can be enhanced for the electrocatalysis of the OER when $[Cr(C_2O_4)_3]^{3-}$ is introduced by intercalation.[39] The weak electronegativity of Cr^{3+} leads to electron-rich Fe sites and higher valence states of Ni which in turn enhances the catalytic properties of the material. Park *et al.* have reported excellent electrocatalytic properties of a ternary LDH, NiFeCo-LDH, developed for alkaline anion exchange membrane (AEM) seawater electrolysers.[40] The compound showed 249 mV overpotential at 10 mA cm^{-2} in 1 M KOH and the seawater electrolyser showed a high performance (0.84 A cm^{-2} at 1.7 V$_{cell}$) and a high efficiency (77.6% at 0.5 A cm^{-2}) for seawater electrolysis. In addition to LDH materials other compounds with similar structures are widely studied. These include compounds such as NiO/NiOOH,[41–43] $Fe(OH)_2$/FeOOH,[44] $Co(OH)_2$/CoOOH,[45] $Ni(OH)_2$/NiOOH,[46–49] which have been reported to have comparable OER performance in alkaline conditions. However, it was later discovered that LDH phases were responsible for the OER electrocatalysis, ascribed to their formation in OER conditions.[50–53] In general, LDH materials have proven to be very efficient for the electrochemical and photochemical OER, and such materials have been extensively reviewed elsewhere.[38,54–56] Similarly, transition metal dichalcogenides (TMDC), such as MoS_2, have been proposed as good alternatives as electrocatalysts for the OER. Having a general formula MX_2, with M being a transition metal and the chalcogenide X = S, Se or Te, these materials feature transition metal sandwiched between two chalcogenide layers (see Figure 4b). Their properties have been extensively reviewed for the OER elsewhere.[56–58]

Li-rich cathode materials have become widely researched and commercially employed for lithium-ion batteries (LIBs).[59] However, gas evolution, *i.e.* O_2, CO_2, H_2 and ethylene, during the operation of LIBs at high voltages, is one of their most significant failure mechanisms.[60] Lithium-layered cathode materials, such as $LiCoO_2$, can be used for the OER when employed in aqueous electrolytes. In general, Li-containing oxides have been shown to have potential in modulating the properties of metal oxide catalysts and interest is growing in Li-layered mono and polymetallic oxide electrocatalysts as tuneable materials. In this review we aim to provide a summary of alkali metal-layered electrocatalysts for the OER with a focus on recently published reports. To the best of our knowledge, no publications have reviewed such lithium- and other alkali metal-layered electrocatalysts for the OER. Herein, we present the main findings on structure, morphology, electronic structure, catalytic activity and stability towards OER for this class of materials.
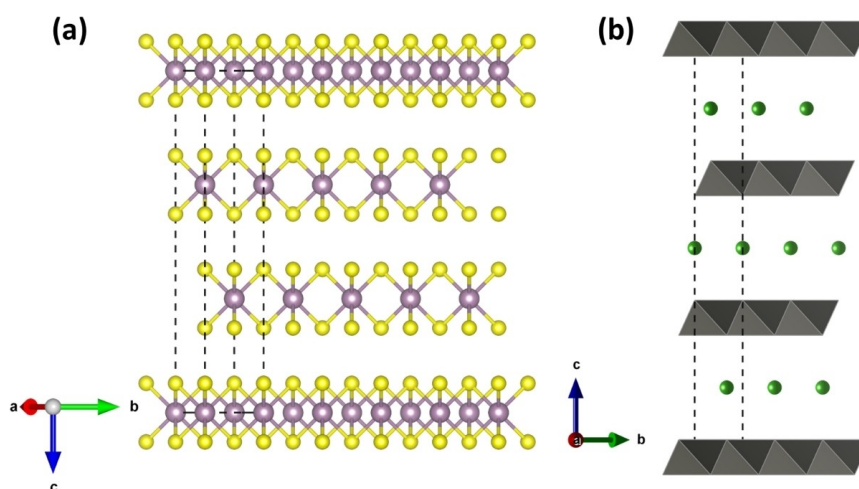
Figure 4. Layered crystal structures of a (a) MoS_2 (Mo atoms in violet and S in yellow) as a representative structure for TMDCs and (b) $M^{2+}_{1-x}M^{3+}_x(OH)_2(A^{n-})_{x/n} \cdot yH_2O$ LHD structure ($M^{2+/3+}$ represented by grey polyhedra and A^{n-} represented by green atoms).

ChemElectroChem

Review
doi.org/10.1002/celc.202300761

**Chemistry
Europe**
European Chemical
Societies Publishing

2. Layered Cobalt-based oxides

2.1. Lithium Cobalt Oxide - Li_2CoO_2

Among layered materials, lithium-containing compounds are commonly studied as energy storage technologies. Lithium Cobalt Oxide ($LiCoO_2$) is regarded as one of the most important materials in modern society due to its high energy density and stability making it an ideal cathode material for energy storage.[61] $LiCoO_2$ belongs to a class of material usually referred to as lithium-mediated metal oxides (LMOs), which have been found to be active towards the OER in alkaline or neutral conditions. The introduction or removal of lithium ions to the lattice induces changes in surface and electronic structure, resulting in modulation of electrocatalytic performance.[62]

Submicrometric particles of $LiCoO_2$ with a layered trigonal $R\bar{3}m$ structure (Figure 5a and 5b for crystal structure and powder XRD pattern), were investigated by Lee *et al.* in neutral and alkaline conditions using a three-electrode setup with a glassy carbon (GC) ring disk electrode (RDE), a Ag/AgCl reference electrode and a Pt-mesh counter electrode, specifically at pH 7 and 13 (prepared with 0.1 M KH_2PO_4 and KOH, respectively). It was shown that the OER activity, surface morphology and composition undergo significant changes when the electrocatalyst is cycled in/out the OER region (see Figure 5c).[63] During one cyclic voltammetry (CV) at pH 7, $LiCoO_2$ showed a large anodic peak with ~1.3 V_{RHE}, attributed to the oxidation of cobalt within the electrocatalyst coupled with delithiation. A

second CV scan showed further anodic features at ~1.6 V_{RHE} ascribed to the OER process. The activity towards the OER gradually decreased with the increasing number of potential cycles, indicating deactivation of the electrocatalyst, attributed to changes in surface morphology and composition. As shown in Figure 5c, high-resolution transmission electron microscopy (HR-TEM) and fast fourier-transfrom (FFT) images showed that after 100 CV scans, the surface of $LiCoO_2$ transitions to a spinel-like $LiCo_2O_4$ phase, which features a lower density of active sites leading to lower activity. Interestingly, when cycled in alkaline conditions (pH 13), $LiCoO_2$ was been found to become amorphous.[63] Interestingly, no increase in activity is observed when the material is employed at pH 13 despite its amorphization. However, differences at quasi-steady-state OER conditions are observed, as indicated by the calculated Tafel slopes of ~120 and ~60 mV dec^{-1} at pH 7 and 13, respectively. This study demonstrates how the presence of lithium as an interlayer species and deintercalation processes can significantly alter the electrocatalytic properties towards the OER and how the observation of pH-dependent surface changes following deintercalation highlights the importance of understanding and controlling the restructuring of the surface during catalyst evolution.

Lu *et al.* prepared $LiCoO_2$ *via* soaking cotton in solutions of $LiNO_3$ and $Co(NO_3)_2$ follow by oxidative heat treatment to up to 400 °C.[64] The resulting material was slowly heated and held at 850 °C for 4 h. Subsequently, $Li_{0.5}CoO_2$ was prepared by loading $LiCoO_2$ electrodes in a battery cell and employing $LiPF_6$ in ethylene carbonate and diethyl carbonate electrolyte (EC/DEC) as an organic electrolyte mixture to achieve controlled lithium deintercalation, leading to a well-structured delithiated cobalt oxide. It was found that delithiation of $LiCoO_2$ to $Li_{0.5}CoO_2$ prior to its application as an electrocatalyst for the OER in alkaline conditions leads to enhanced electrocatalytic activity, a phenomenon attributed to the specific electronic structure of the delithiated compound.[64] XRD measurements show that $Li_{0.5}CoO_2$ adopts a monoclinic structure and the low angle reflections shift to a higher angle due to a hexagonal to monoclinic structural transition on the formation of $Li_{0.5}CoO_2$. XPS analysis suggested that the average Co oxidation state in $Li_{0.5}CoO_2$ is higher than 3^+. Such structural and oxidation state changes were only observed in organic lithium-containing electrolytes suitable for conducting lithiation/delithiation experiments rather than aqueous alkaline electrolyte, such as KOH. Therefore, such properties are preserved in aqueous electrolyte when $LiCoO_2$ and delithiated-$LiCoO_2$ are employed for the OER. Scanning electron microscopy (SEM) revealed that no noticeable morphological changes can be observed between $LiCoO_2$ and $Li_{0.5}CoO_2$ (see Figure 6a and 6b). Electrochemical tests were carried out using a GC RDE, a Pt mesh and a saturated calomel electrode (SCE) as the working, counter and reference electrodes respectively, and showed that $Li_{0.5}CoO_2$ has a markedly higher activity than $LiCoO_2$ towards OER in the aqueous KOH electrolyte, with such enhanced properties ascribed to specific crystal structures and oxidation states achieved *via* delithiation. Specifically, the onset potential is reduced with lower Li concentration, *i.e.* ~1.59 V and ~1.52 V
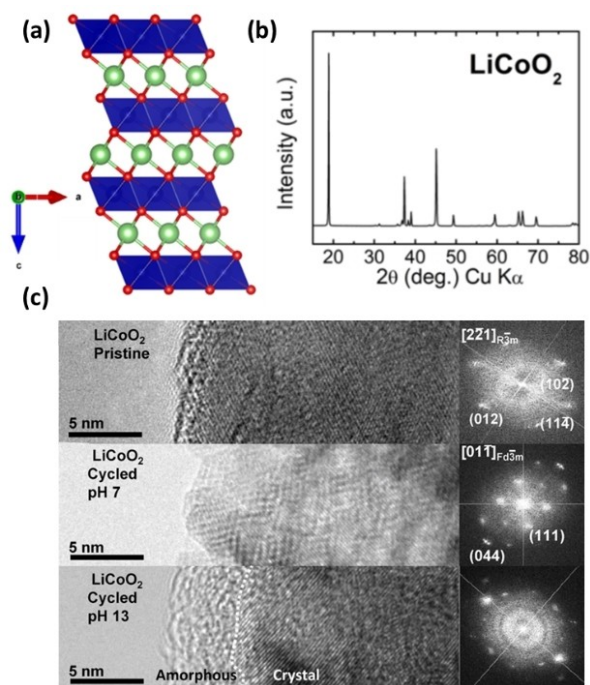
Figure 5. (a) Layered crystal structure of $LiCoO_2$ showed along the *b*-axis and (b) corresponding powder X-ray diffraction pattern of $LiCoO_2$. (c) HR-TEM and corresponding FFT images of pristine $LiCoO_2$ and after cycling at pH 7 and pH 13, clearly showing a transition to a spinel-like phase and an amorphous phase, respectively. Adapted with permission from *J. Am. Chem. Soc.* 2012, 134, 41, 16959–16962. Copyright 2012 American Chemical Society.

ChemElectroChem

Review
doi.org/10.1002/celc.202300761

Chemistry
Europe
European Chemical
Societies Publishing
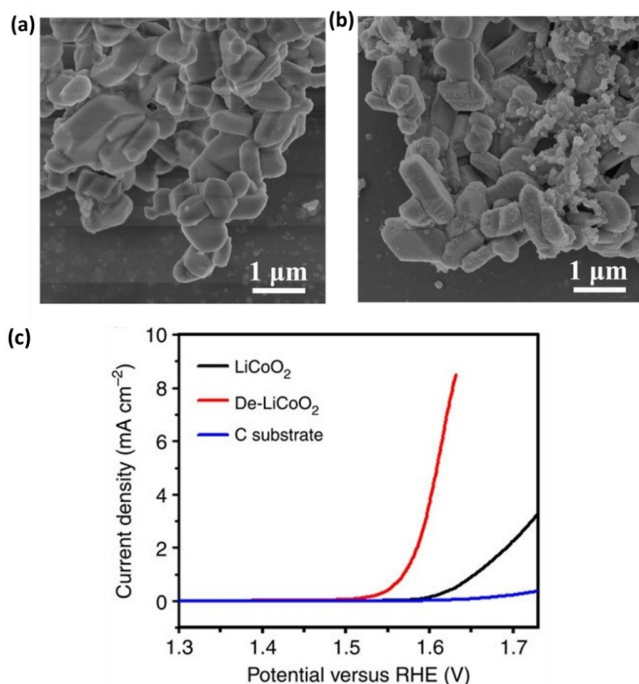
Figure 6. SEM images of $LiCoO_2$ (a) before and (b) after electrochemical tuning. The similar size and morphology of $LiCoO_2$ and delithiated-$LiCoO_2$ indicate the improved OER performance of the latter is not ascribable to size and morphological effects.(c) Linear scanning voltammetry curves of $LiCoO_2$, delithiated $LiCoO_2$ and the carbon substrate, showing the delithiated electrocatalyst features enhanced OER activity in alkaline electrolyte. Reproduced from ref.[64] with permission from Springer Nature.

for $LiCoO_2$ and $Li_{0.5}CoO_2$, respectively. Furthermore, $Li_{0.5}CoO_2$ shows a higher current density at higher applied overpotentials compared to $LiCoO_2$ as shown by linear scanning voltammetry (LSV) measurements (see Figure 6c). However, estimating the effective surface area via electric double-layer capacitance (C_{DL}) showed that $Li_{0.5}CoO_2$ has higher C_{DL} by almost two orders of magnitude after delithiation, i.e. ~60 versus ~2000 µF cm^{-2} for $LiCoO_2$ and $Li_{0.5}CoO_2$, respectively. This indicates that the latter compound exhibits a higher electrochemically active surface area resulting in the exposure of a greater population of active

sites supporting higher activity towards the OER. The enhanced activity observed for $Li_{0.5}CoO_2$ was attributed to (i) the increased oxidation state of Co, leading to higher electrophilicity of the adsorbed O for a OH- anion in the electrolyte to form -OOH species, (ii) the increase in the covalent character of the Co—O bond following delithiation, which may lead to the formation of holes in the hybridised Co 3d-O 2p orbitals, potentially facilitating the affinity of the electrocatalyst for OH$^-$ groups and (iii) the more metallic character of $Li_{0.5}CoO_2$ compared to $LiCoO_2$, the latter showing semiconductor behaviour.[65] Furthermore, this study has also shown the polarization curve of the delithiated-$LiCoO_2$ after 1,000 cycles has negligible loss of anodic current compared to the first cycle, and a stable current of ~10 mA cm^{-2} was recorded for more than 2 h of operation.[64] Therefore, this study has shown how the performance of $LiCoO_2$ can be improved by a process of delithiation, suggesting this is a viable way to fine-tune the properties of layered electrocatalysts.

2.2. Li-layered Co-based alloy oxides

The OER is an unwanted side reaction in NiO_x alkaline batteries, and it has long been found that Fe impurities enhance such a process,[66–69] with this attracting significant attention to the effects of Fe-doping in NiO_x electrodes for OER electrocatalysis in alkaline media. Many studies have indeed shown that Fe-doped nickel oxides are promising electrocatalysts for the OER.[70–74] Similar to Fe-doped nickel oxides, the effect of Fe-doping in Li-layered metal oxides as electrocatalysts for the OER has been investigated. A series of Co-based oxides, $LiCo_{1-x}M_xO_2$ (M = Ni, Fe and Mn) was also investigated by Lu et al. using the same preparation methods as for $LiCoO_2$ and $Li_{0.5}CoO_2$.[64] First, pristine $LiCo_{0.5}Ni_{0.5}O_2$, $LiCo_{0.5}Fe_{0.5}O_2$, $LiCo_{0.33}Ni_{0.33}O_2$ and $LiCo_{0.33}Fe_{0.33}O_2$ were synthesised. It was found that all these electrocatalysts featured the same crystalline structure as $LiCoO_2$ and showed slightly improved or comparative OER activity compared to $LiCoO_2$ (see Figure 7a and 7b). Following the same delithiation procedure in non-aqueous lithium-containing electrolyte ($LiPF_6$ in ethylene carbonate and diethyl
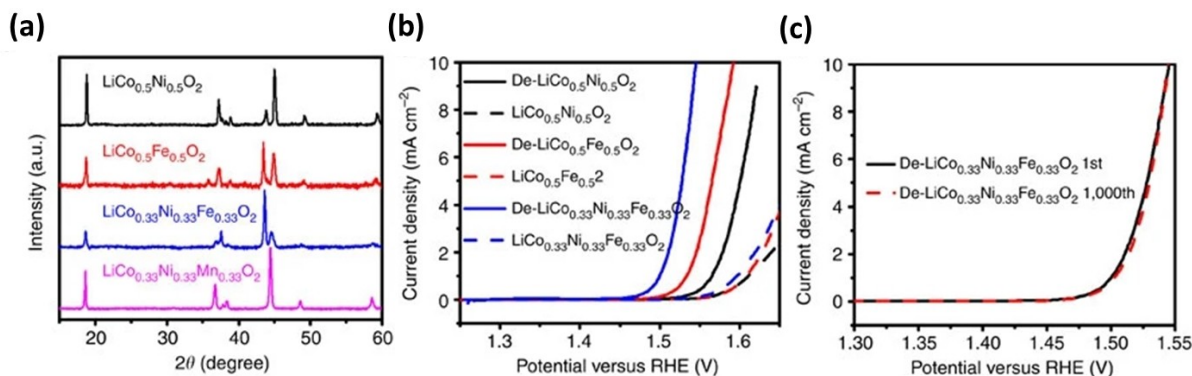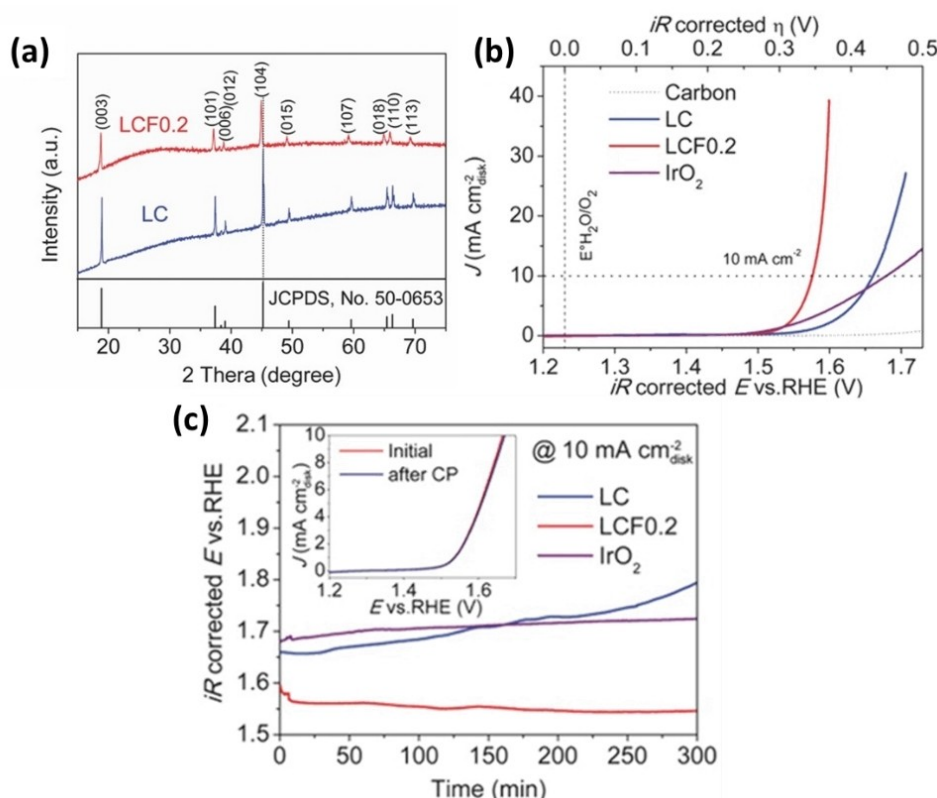

Figure 7. (a) Powder X-ray diffraction patterns for $LiCo_{0.5}Ni_{0.5}O_2$, $LiCo_{0.5}Fe_{0.5}O_2$, $LiCo_{0.33}Ni_{0.33}Fe_{0.33}O_2$ and $LiCo_{0.33}Ni_{0.33}Mn_{0.33}O_2$. (b) LSV curves of mixed lithium transition metal oxides before and after delithiation. (c) Cycling stability of the De-$LiCo_{0.33}Ni_{0.33}Fe_{0.33}O_2$ catalyst. Adapted from ref.[64] with permission by Springer Nature.

ChemElectroChem

Review
doi.org/10.1002/celc.202300761

Chemistry
Europe
European Chemical
Societies Publishing

carbonate), the delithiated electrocatalysts showed improved OER properties compared to $LiCoO_2$ and $Li_{0.5}CoO_2$, when tested in 0.1 M KOH using a three-electrode setup comprising carbon fibre paper, a Pt wire and Hg/HgO as the working, counter and reference electrodes, respectively. Firstly, the onset potential decreased by around 30–80 mV, in addition the Tafel slopes were shown to be similar or reduced, suggesting the OER kinetics are not negatively affected by substitution of Co for of Ni and Fe. CV measurements for 1000 cycles revealed such delithiated samples also possess high stability, as shown by delithiated-$LiCo_{0.33}Ni_{0.33}FeO_{0.33}O_2$ (see Figure 7c). Overall, the study reported by Lu *et al.* highlighted the effects of delithiation in Li-layered Co-based oxides as a method to increase activity by increasing electrochemical surface area, however the effect was only observed when delithiation was carried out in non-aqueous electrolytes due to changes in crystal structure and oxidation states that are not observed in aqueous alkaline electrolytes.

Zhu *et al.* found a similar enhancement of the OER activity of Co-based mixed metal oxides such as $LiCo_{0.8}Fe_{0.2}O_2$, synthesised using a sol–gel process.[75] XRD measurements showed that $LiCo_{0.8}Fe_{0.2}O_2$ retains the layered $R\bar{3}m$ structure of $LiCoO_2$, with some increased lattice parameters because of the higher Fe ionic radius leading to lattice expansion (see Figure 8a). HR-TEM and electron diffraction (ED) measurements corroborated such

structural properties, further indicating a Li-layered structure with Co and Fe occupying octahedral sites. SEM measurements revealed $LiCo_{0.8}Fe_{0.2}O_2$ formed bigger particle agglomerates compared to $LiCoO_2$, suggesting Fe doping might lead to better interconnection and intergrowth of particles. Electrochemical tests were carried out in 0.1 M KOH using a GC RDE, a Pt foil and Ag/AgCl (3.5 M KCl) as working, counter and reference electrodes, respectively. LSV curves obtained for $LiCo_{0.8}Fe_{0.2}O_2$ (denoted as LCF0.2) in alkaline conditions (0.1 M KOH) clearly showed that this catalyst exhibits a lower onset potential than the parent $LiCoO_2$, and higher catalytic activity (see Figure 8b). In addition, $LiCo_{0.8}Fe_{0.2}O_2$ also shows higher current densities than IrO_2 in this pH range (despite a lower onset potential, *i.e.* 1.47 V) therefore outperforming this benchmark electrocatalyst. Chronopotentiometry (CP) measurements to probe the stability of $LiCo_{0.8}Fe_{0.2}O_2$ showed a stable performance over 5 h by maintaining a potential of 1.57 V at 10 mA cm^{-2} (Figure 8c), longer tests conducted to up to 10 h showed little increases in potential. By contrast, $LiCoO_2$ and IrO_2 when used as reference electrocatalysts under the same experimental conditions show much larger variation in operational potentials over time. The lower stability of $LiCoO_2$ without delithiation was ascribed to the loss of Li during the OER, which led to the formation of a Li-deficient Co_3O_4-like surface. The $LiCo_{0.8}Fe_{0.2}O_2$ CV and LSV measurements also indicate that a similar Li loss occurs in the

Figure 8. (a) Powder X-ray diffraction patterns of $LiCoO_2$ (LC, blue curve), $LiCo_{0.8}Fe_{0.2}O_2$ (LCF0.2). (b) LSV measurements the RDE comprised of the $LiCoO_2$ (LC), $LiCo_{0.8}Fe_{0.2}O_2$ (LCF0.2), and IrO_2 catalysts in O_2-saturated 0.1 M KOH solution. The background OER activity of a Nafion-bonded carbon thin film electrode is used as a reference. (c) CP measurements of the LC, LCF0.2, and IrO_2 catalysts at a constant current density of 10 mA cm^{-2} disk in O_2-saturated 0.1 M KOH. The inset shows the LSV curves of the LCF0.2 catalyst before and after the CP test (scan rate: 5 mV s^{-1}). Adapted from ref.[75] with permission from John Wiley and Sons.

ChemElectroChem

Review
doi.org/10.1002/celc.202300761

**Chemistry
Europe**
European Chemical
Societies Publishing

doped materials, but Fe doping plays a key role in maintaining the electrocatalyst's stability for prolonged use. XPS measurements suggest that Fe doping affects the electronic properties of the surface Co ions, indicating partial oxidation of the surface Co species from Co^{3+} to Co^{4+}, thus enhancing the electrophilicity of absorbed O and its affinity to OH^- species to form adsorbed $-OOH$ species. Secondly, XPS revealed that Fe doping increased the concentration of O_2^{2-} and O^- species formed on its surface which have been suggested to be active species in the catalysis of the OER in alkaline electrolytes.[76–78] Furthermore, electrochemical impedance spectroscopy (EIS) of $LiCo_{0.8}Fe_{0.2}O_2$ has demonstrated enhanced charge transfer properties compared to undoped $LiCoO_2$ relating to increased particle interconnection induced by Fe doping. Finally, oxygen temperature programmed desorption (O_2-TPD) measurements have shown that $LiCo_{0.8}Fe_{0.2}O_2$ releases O_2 at significantly lower temperatures than $LiCoO_2$, (518 vs 731 °C), indicating the desorption of the evolved O_2 can be enhanced by Fe doping. This study therefore confirms the higher OER activity and durability of lithium-layered metal oxide electrocatalysts in alkaline conditions compared to benchmark IrO_2 catalysts and further suggests how synergistic effects between Co and Fe are responsible for the enhancement of the activity and stability towards the OER.

The introduction of different alkali metals within layered structures also has the potential to modulate material properties. For instance, $NaCoO_2$, contains sodium cations within the layers of its hexagonal structure. Due to the size and lower mobility of the Na^+, it is possible to obtain stabilised compounds with different Na contents and therefore tune the Co oxidation states of a Na_xCoO_2 (x = 0.75, 0.65, 0.52, 0.36) family of electrocatalysts while maintaining the hexagonal crystalline structure (see Figure 9a),[79] with Na_xCoO_2 also being a well-known semiconductor in its hydrated form.[80] $Na_{0.75}CoO_2$ was first synthesised *via* a sol-gel method, and the other members of the Na_xCoO_2 family were prepared *via* sodium deintercalation of $Na_{0.75}CoO_2$. Such a deintercalation process has been shown to result in the expansion of the two-dimensional CoO_2 layers because of electrostatic repulsion and forms a double-layer hydrated compound, $Na_xCoO_2 \cdot 1.3H_2O$,

when the concentration of Na < 0.4 (see Figure 9a). Electrocatalytic tests using a GC RDE, a Pt mesh and KCl-saturated Ag/AgCl as working, counter and reference electrodes, respectively, showed that the activity of the Na_xCoO_2 compounds increases with decreasing Na concentration following deintercalation (see Figure 9b). CV curves show currents from ~30 to ~50 mA cm^{-2} for x = 0.75 and 0.36, respectively, and a significant decrease in onset potential for the OER. Furthermore, overpotentials for Na_xCoO_2 at 10 mA cm^{-2}, were found to be 415, 445, 450 and 470 mV for x = 0.36, 0.52, 0.65 and 0.75, respectively. Notably, $Na_{0.36}CoO_2$ has a lower overpotential at 10 mA cm^{-2} than $LiCoO_2$ (cf. ~430 mV). However, Tafel analysis of all the electrocatalysts gives rise to similar slopes, *i.e.* ~41 mV dec^{-1}, and are comparable to that of $LiCoO_2$,[81] suggesting the kinetically relevant reaction steps remain unaltered. CV measurements show that $Na_{0.36}CoO_2$ and $Na_{0.52}CoO_2$ can operate for 50 cycles with no indication of degradation, whereas compounds with higher Na^+ content slowly increase in activity and stabilise to current densities comparable to that of $Na_{0.52}CoO_2$ (see Figure 9c). This suggests that for higher Na^+ concentrations, Na deintercalation occurs easily during the OER catalysis. Detailed XPS studies have shown such differences in electrocatalytic properties have been attributed to the increase of surface Co(III)/Co(IV) ratio upon deintercalation of the Na cation and the resulting formation of oxygen vacancies on the surface of the electrocatalysts, which play an important role as active sites in OER catalysis.[79] Such results therefore highlighted how other alkali metals can also be employed to enhance the performance of electrocatalysts for the OER and provide further guidance on the rational design of catalysts.

In 2017, Weng *et al.* have reported a series of $NaCo_yFe_{1-y}O_2$ electrocatalysts,[82] albeit these served as a comparison for Ni-containing $NaNi_yFe_{1-y}O_2$ analogues, which were the main focus of the study and will be discussed later in this review. The $NaCo_yFe_{1-y}O_2$ compounds adopt a hexagonal O3-type structure of $R\bar{3}m$ space group, similar to the catalysts previously discussed (see Figure 10a). It is shown *via* testing in 1 M KOH using a GC RDE, a Pt foil and Ag/AgCl as working, counter and reference electrodes, respectively, that $NaCo_{0.8}Fe_{0.2}O_2$ was the optimal reported composition among the $NaCo_yFe_{1-y}O_2$ catalysts
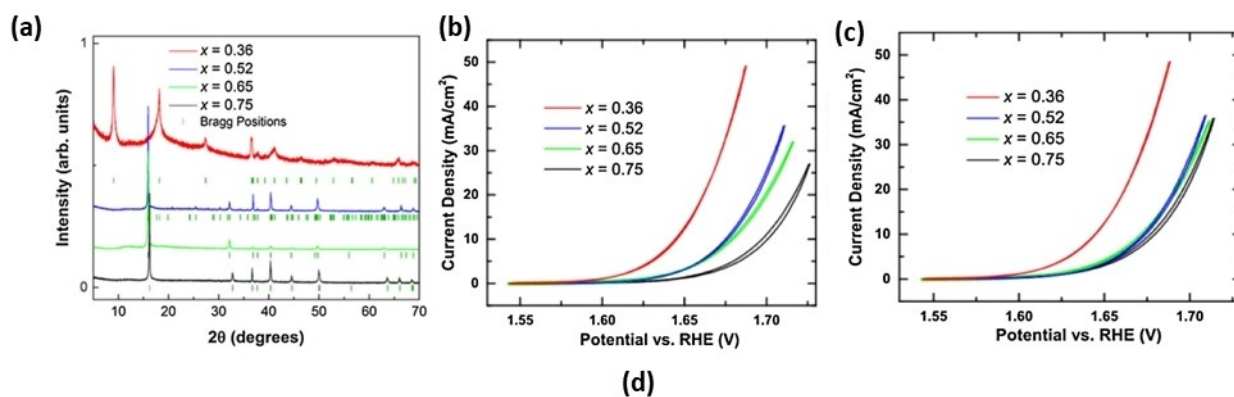
Figure 9. (a) Powder X-ray diffraction patterns for Na_xCoO_2 (x = 0.36, 0.52, 0.65, 0.75) and Bragg positions. (b) 2nd CV scan for the Na_xCoO_2 compounds and (c) 50th CV scan. Adapted with permission from Ref.[79]
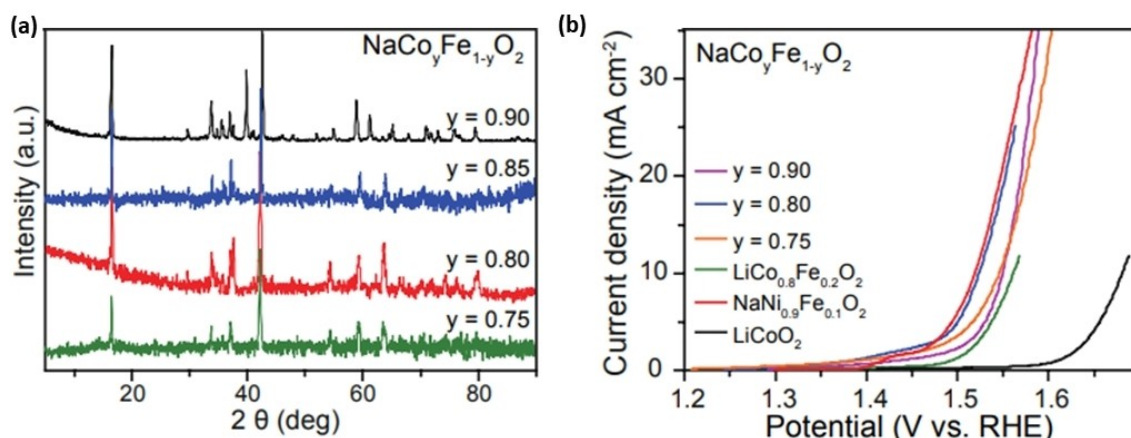
Figure 10. (a) Powder X-ray diffraction patterns for $NaCo_yFe_{1-x}O_2$ ($x = 0.75$, 0.80, 0.85, 0.75) and (b) LSV scans in 1 M KOH. Reproduced from Ref.[82] with permission from the Royal Society of Chemistry.

and outperforms noble metal electrocatalysts, including RuO_2 (see Figure 10b). In particular, $NaCo_{0.8}Fe_{0.2}O_2$ required a potential of $1.56\ V_{RHE}$ to generate $10\ mA\,cm^{-2}$ and Tafel slope of $45\ mV\,dec^{-1}$, whereas RuO_2 measured with similar loadings exhibited a potential of $1.58\ V_{RHE}$ to reach $10\ mA\,cm^{-2}$ and a Tafel slope of $73\ mV\,dec^{-1}$. Unfortunately, unlike the $NaNi_yFe_{1-y}O_2$ family of electrocatalysts, no further physicochemical characterisation has been conducted for this Co-containing series and, to the best of our knowledge, no further information is available for this series of compounds despite their promising performance.

3. Layered chromium and nickel-based oxides

3.1. LiCrFeO₂

To date, little work has been reported concerning chromium-rich electrocatalysts towards OER. Recently, Soni *et al.* obtained a family of layered $Li_yCr_{1-x}Fe_xO_2$ ($y \leq 1$, $0 \leq x \leq 0.2$) *via* a solid-state ceramic synthesis.[83] These compounds adopt a layered rhombohedral structure in the $R\bar{3}m$ space group with 2.5 Å interplanar *d*-spacing. HR-TEM and a combination of X-ray and electron diffraction measurements suggest that Fe acts as a dopant and Li cations sit between mixed Cr/Fe two-dimensional layers. Further XRD measurements show that up to 10% Fe can replace Cr atoms in $LiCrO_2$, with higher concentrations of Fe leading to the formation of Fe_2O_3. Rietveld analysis of the XRD patterns has also shown that Cr atoms can intermix in the Li layers with increasing concentrations of Fe. XPS shows that one of the peculiarities of these Cr-rich electrocatalysts lies in the ability of Cr to adopt different oxidation states, *i.e.* $+3, +4$ and $+6$ and Fe-doping promotes Cr^{6+} species. While Li^+, Cr^{3+} and Cr^{4+} adopt an octahedral coordination geometry, Cr^{6+} units adopt a tetrahedral geometry. Due to the presence of Li vacancies, these Cr^{6+} ions occupy interstitial sites in the Li layers, leading to the formation of dumbbell defects. Dumbbell defects are interstitial defects where two atoms share the same lattice site and have a "split" structure (see Figure 11a). When

tested for the OER using carbon paper, Ag/AgCl (4 M KOH) and a Pt wire as working, reference and counter electrodes, respectively, the electrocatalytic activity was shown to increase with the increasing concentration of Fe up to 10% and to decrease for higher Fe content. $Li_{0.6}Cr_{0.9}Fe_{0.1}O_2$ was therefore found to exhibit the highest current density (see Figure 11b), with $28\ mA\,cm^{-2}$ achieved at a 350 mV overpotential – approximately twice that observed for commercial RuO_2 at the same potential, *i.e.* $13\ mA\,cm^{-2}$ and a 311 mV overpotential at $10\ mA\,cm^{-2}$. For other $Li_yCr_{1-x}Fe_xO_2$ electrocatalysts, overpotential at $10\ mA\,cm^{-2}$ were found to be 374, 347, 364 and 383 mV for $x = 0.00$, 0.05, 0.15, 0.20, respectively. Tafel analysis shows that reaction kinetics are faster for $Li_{0.6}Cr_{0.9}Fe_{0.1}O_2$ due to its lowest Tafel slope of $50\ mV\,dec^{-1}$ compared to the Tafel slopes measured the other electrocatalysts, namely 74, 57, 70, and $65\ mV\,dec^{-1}$ for $x=0$, 0.05, 0.15 and 0.20 (see Figure 11c). These results, combined with studies on charge transfer properties of the $Li_yCr_{1-x}Fe_xO_2$ compounds indicating faster charge transfer kinetics when $x = 0.10$, compared to RuO_2 in alkaline electrolyte (1 M KOH), the latter requiring an overpotential of 336 mV to reach a current density of $10\ mA\,cm^{-2}$ and exhibiting lower current densities, a higher Tafel slope ($87\ mV\,dec^{-1}$) and lower charge transfer kinetics. Chronoamperometry (CA) measurements were carried out at $1.54\ V_{RHE}$ for 12 h to assess the stability of $Li_{0.6}Cr_{0.9}Fe_{0.1}O_2$, current density increases for the first few hours and then stabilises for the remainder of the stability test (see Figure 11d). A thousand cycles of CV scans confirmed such a stability by showing only marginal changes in the overpotential at $10\ mA\,cm^{-2}$ for $Li_{0.6}Cr_{0.9}Fe_{0.1}O_2$ up to the 1000th scan. (see Figure 11d inset).

The delithiation process in $Li_{0.6}Cr_{0.9}Fe_{0.1}O_2$ was investigated by focusing on pre-OER redox features at 1.15 and $1.55\ V_{RHE}$ *via* CV scans. Features observed at ~1.42 and ~1.33 V_{RHE} the oxidation of Cr^{3+} to Cr^{6+} – which leads to Li deficiency – and CV curves indicate such peaks increase with Fe doping, with $Li_{0.6}Cr_{0.9}Fe_{0.1}O_2$ featuring the most significant features. This indicates that 3-electron transfer processes are easier in a single redox event in $Li_{0.6}Cr_{0.9}Fe_{0.1}O_2$ compared to the other electrocatalysts in the $Li_yCr_{1-x}Fe_xO_2$ series. Such an enhanced catalytic
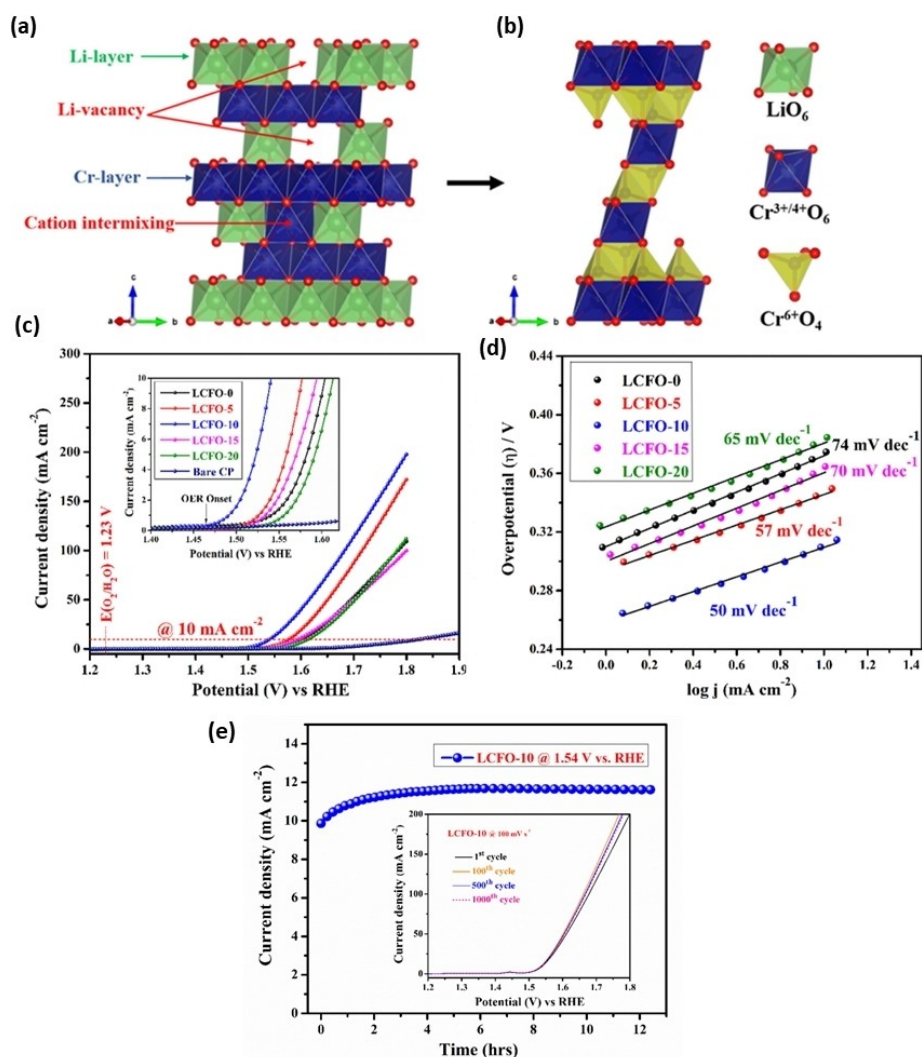
Figure 11. (a,b) Crystal structure of Fe-doped $LiCrO_2$ layered structure and interstitial Cr^{6+} ion-occupied dumbbell defect-containing structure. (c) LSV measured at a scan rate of 5 mV s^{-1} in 1 M KOH. (d) Tafel plots. (e) Chronoamperogram of $Li_{0.6}Cr_{0.9}Fe_{0.1}O_2$ showing stability up to 12 h, with inset showing CV scans of up to 1000 cycles. Adapted with permission from *ACS Appl. Energy Mater.* 2023, 6, 3, 1308–1320. Copyright 2023 American Chemical Society.[83]

activity of $Li_{0.6}Cr_{0.9}Fe_{0.1}O_2$ towards OER has been ascribed to the synergistic interaction between Cr and Fe sites and the high-valence state of Cr^{6+}, which favours the absorption of OH$^-$ species and facilitates the formation of Cr—O—OH bonds. Overall, Soni *et al.* have highlighted how the significant enhancement of the electrocatalytic performance towards the OER is achieved due to the synergistic play between Cr^{6+} and Fe^{3+} ions in the crystal structure and highlights how defects – such as the dumbbell defects – can play a significant role in determining the oxidation state of transition metals, such as Cr^{6+}, in OER electrocatalysts.

3.2. Layered LiNiO$_x$

Gupta *et al.* conducted a systematic study on the OER of $LiNiO_2$ and $LiNi_{1-x}Al_xO_2$ family of electrocatalysts where Al is introduced as a dopant *via* both solution combustion and solid-state synthesis methods, showing that electrocatalysts fabricated with the former method all exhibit lower overpotentials.[84] Specifically, $LiNiO_2$ was shown to exhibit a high mass-normalised current density (~520 mA mg^{-1}$_{oxide}$) with an over-potential of ~330 mV when tested using a GC RDE, a Ag/AgCl (1 M KCl) and a Pt wire as working, reference and counter electrodes, respectively in a 0.1 M KOH electrolyte (see Figure 12a). Upon increasing the concentration of Al up to 20%, enhancements of the current densities were observed along with a reduced onset potential. However, the performance of the electrocatalysts decreased for higher concentrations of Al. Among these materials, $LiNi_{0.8}Al_{0.2}O_2$ shows the best performance, with an activity comparable to that of commercial rutile IrO_2, *i.e.* above 800 mA mg^{-1}$_{oxide}$. In particular, it was shown that high Ni oxidation states are responsible for the enhancement of the activity, *i.e.* a higher Ni(IV)/Ni(III) ratio and removal of Ni(II) species, favoured by low-temperature combustion synthesis ($T < 650$ °) which prevents the reduction of Ni(III) to Ni(II), the latter typically due to the formation of oxygen vacancies at higher temperatures. The stability of this electrocatalyst was
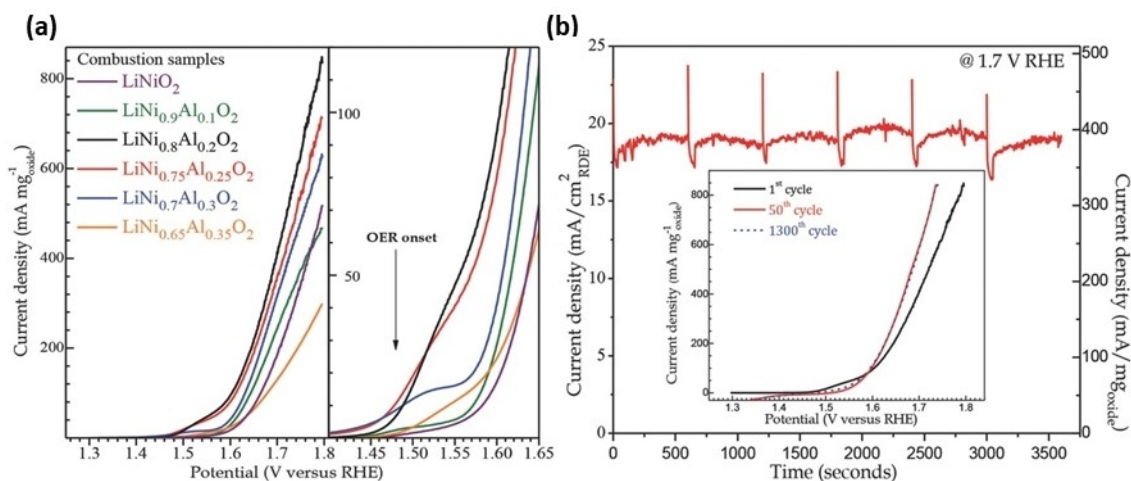
Figure 12. (a) LSV curves for $LiNiO_2$ and $LiNi_{1-x}Al_xO_2$ ($x = 0.1, 0.2, 0.25, 0.3, 0.35$) showing the OER performances of these electrocatalysts and their OER onset. (b) Chronoamperometry measured to assess the stability of $LiNi_{0.8}Al_{0.2}O_2$ and CV measurements during 1st, 50th and 1300th cycle. ©2015 WILEY-VCH Verlag GmbH & Co. KGaA, Weinheim.

assessed with chronoamperometry and CV measurements showing a stable current density of ~19 mA cm$^{-2}_{geo}$ at 1.7 V$_{RHE}$ for 60 min (see Figure 12b). It is therefore important to note that, as shown by this study show, the synthesis method can affect the oxidation state of the transition metal and how Ni and Al play a synergistic role as shown for layered cobalt oxide catalysts.

A more in-depth study on the effect of doping in similar Ni-rich structures had been conducted by Augustyn et al.[85] The members of the $LiNi_{1-x}M_xO_2$ ($M = $ Mn, Fe, Co) family of electrocatalysts feature a Li-layered rhombohedral structure.[85] In particular, Fe-doping is responsible for the most significant improvement of catalytic properties towards OER in these $LiNi_{1-x}M_xO_2$ compounds, with this effect attributed to the ability of surface Fe to easily adopt different coordination geometries. When tested in 0.1 M KOH using a GC RDE, a Pt mesh and a SCE as working, counter and reference electrodes, respectively, the most active electrocatalysts tested was $LiNi_{0.7}Co_{0.3}Fe_{0.2}O_2$, with a

maximum current density of ~100 mA mg$^{-1}_{oxide}$ at a 379 mV overpotential (see Figure 13).[85] Following chemical delithiation of the electrocatalysts, it was shown that delithiation alters the oxidation state of the transition metal cations and also induces changes in the morphologies of the samples and the surface area, as measured via SEM and Braun-Emmet-Taller (BET) measurements. While mass normalised activities tend to converge to similar values, BET normalised activities show that the delithiated compounds perform worse than the as-synthesised materials. CV measurements have shown additional cathodic peaks compared to the chemically delithiated samples, ascribed to in situ lithium intercalation/deintercalation during the first OER cycles and therefore indicating that such phenomenon does not occur in already delithiated electrocatalysts. Therefore, it has here been highlighted how properties such as morphology, surface area and local chemical environment induced by chemical delithiation severely affect the OER performance and stress the important role of
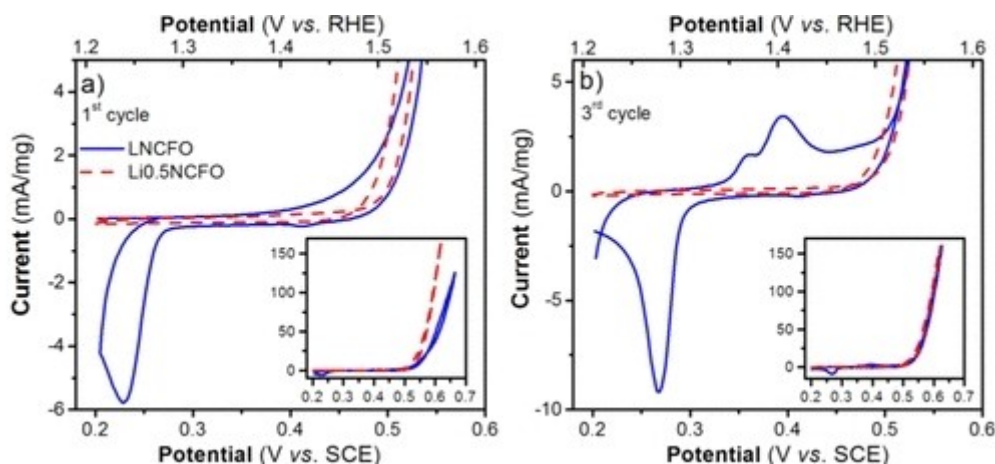

Figure 13. RDE CVs at 10 mV s^{-1} and 1600 rpm in 0.1 M KOH for LNCFO and Li0.5NCFO for (a) the first cycle and (b) the third cycle (the insets show the entire potential region). Adapted with permission from J. Phys. Chem. Lett. 2015, 6, 19, 3787–3791. Copyright 2015 American Chemical Society.

ChemElectroChem

Review
doi.org/10.1002/celc.202300761

Chemistry
Europe
European Chemical
Societies Publishing

morphological and structural changes in determining the electrocatalytic properties of such materials towards the OER beyond the simple change in oxidation states of the transition metals.

Fu *et al.* reported $Li_xNi_{1-x}O$ with $x > 0.3$ transitions from a cubic to rhombohedral phase with the distribution of Ni and Li ions into respective layers.[36] XPS experiments suggest that oxygen vacancies increase linearly with Ni(III)/Ni(II) ratio on the surface of the catalyst, albeit only for $x \leq 0.3$, followed by a decrease for $x > 0.3$. Electrochemical measurements, using a rotating ring disk as a working electrode in alkaline conditions (0.5 M NaOH), a Pt-wire counter electrode and a Hg/HgO (1 M KOH) as a reference electrode, have shown that $Li_{0.3}Ni_{0.7}O$ demonstrates the highest activity towards OER with this declining activity at higher concentration of Li ascribed to the decreasing number of Ni^{3+} sites (see Figure 14). These results were corroborated *via* DFT calculations showing that O 2p-Ni 3d hybridisation near the Fermi level is enhanced by the presence of Li, with also creates new hole states. Both factors optimise the adsorption of OH^- intermediates and enhance the kinetics of the OER. Furthermore, Fu *et al.* have also found that Fe-doping in $LiNi_{0.9}Fe_{0.1}O_2$ leads to a significant increase in electrocatalytic activity and stability, with a current density of $5.16\,mA\,cm^{-2}_{oxide}$ at $1.67\,V_{RHE}$ and a small increase in overpotential after 1000 cycles at the benchmark current density of $10\,mA\,cm^{-2}$.
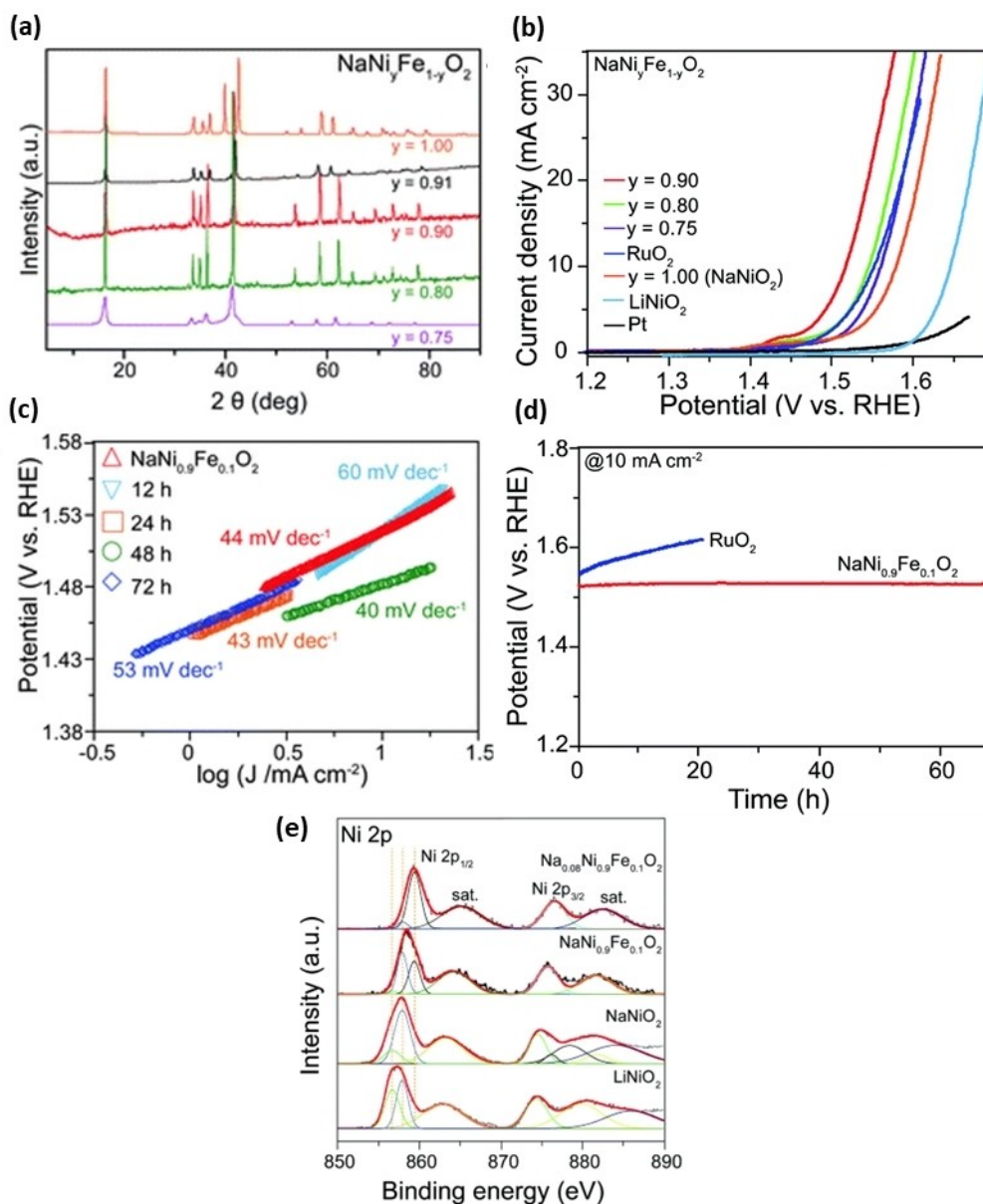
When the lithium content is reduced from $LiNiO_2$ to $Li_{0.69}Ni_{1.31}O_2$, XRD measurements show cation mixing of the Li sites with the Ni sites indicated by a decrease in the reflection centred at 7.5 Å and increase of Ni occupancy in the Li sites *via* Rietveld refinements. Electrocatalytic testing in alkaline electrolyte (0.1 M KOH) shows that $LiNiO_2$ features the lowest onset potential of this catalyst series as cation mixing reduced the activity towards OER. Stability tests conducted at $1.8\,V_{RHE}$ show
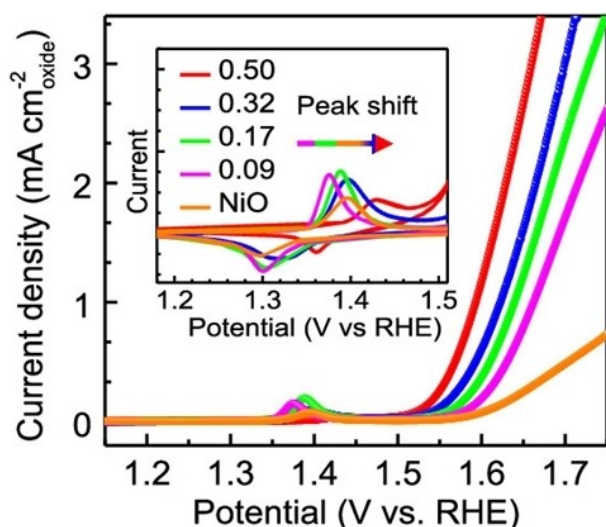
Figure 14. LSV polarization curves of $Li_xNi_{1-x}O$ normalized by the BET surface area in 1 M KOH solution at a scan rate of $10\,mV\,s^{-1}$; inset shows cyclic voltammogram curves at a scan rate of $10\,mV\,s^{-1}$. Adapted with permission from *Chem. Mater.* 2019, 31, 2, 419–428. Copyright 2018 American Chemical Society.

that $LiNiO_2$ exhibits high initial current density, but this rapidly decreases after 10 seconds to the lowest current density among the compounds investigated and is ascribed to Li deintercalation. $Li_{0.69}Ni_{1.31}O_2$ showed by contrast the best stability, attributed to the lower Li diffusion resulting from cation mixing. Interestingly, ICP-OES measurements following stability tests showed that the Li content in $LiNiO_2$ decreased by 85%, whereas $Li_{0.69}Ni_{1.31}O_2$ maintained its composition confirming the poorer stability of $LiNiO_2$ derived from delithiation. Similarly, TEM imaging showed the surface of $Li_{0.69}Ni_{1.31}O_2$ remains unaltered as opposed to that of $LiNiO_2$ for which Ren *et al.* had previously observed the formation of 5–10 nm NiOOH layer after electrolysis.[86] XANES measurements have revealed that decreased cation mixing is responsible for higher concentrations of Ni^{3+} species. EXAFS measurements have also shown that the Ni–O and Ni–Ni distances are shorter with higher Li concentration, *i.e.* 1.93 and 2.87 Å, respectively, for $LiNiO_2$ compared to 1.96 and 2.91 Å for $Li_{0.69}Ni_{1.31}O_2$. XAS measurements of the Ni L-edge and O K-edge can probe the hybridisation of the Ni 3d and O 2p orbitals and revealed that Li-containing materials did not exhibit the characteristic peak of NiO at 532 eV; indicating unoccupied Ni 3d e_g states hybridised with O 2p orbitals. However, an additional feature at 528 eV was observed and this was attributed to the formation of a hole state induced by Li doping confirmed by Ni L-edge XAS measurements which show an extra peak at 857 eV. This feature suggests $3d^7$ and $3d^{8L}$ configurations (L = ligand hole) arise due to the strong covalent character of the bond formed between Ni 3d and O 2p orbitals. *Operando* XANES measurements further confirmed that the instability of $LiNiO_2$ is due to the loss of Li ions as the Ni K-edge of $LiNiO_2$ shifts at higher energies within the first minute of OER and at even higher energies at the end of a 60 min electrolysis procedure. By contrast, the Ni K-edge in $Li_{0.69}Ni_{1.31}O_2$ remains unchanged during such *operando* experiments, suggesting that prevention of lithium diffusion due to cation mixing is indeed a viable method to prevent electrocatalyst degradation. This study clearly shows that Li doping induces changes to the electronic structure of the electrocatalyst, *i.e.* the creation of a new hole state and the higher hybridisation of the Ni–O bond, enhancing the kinetics for the OER.

Weng *et al.* have studied a highly crystalline layered $NaNi_yFe_{1-y}O_2$ double oxides.[82] These catalysts adopt a hexagonal structure of $R\bar{3}m$ space group (see Figure 15a for XRD patterns), where Ni and Fe occupy the same sites and Na replaces the Li in between the layers. Electrochemical studies were carried out using 1.0 M KOH electrolyte and compared to $LiNiO_2$, $NaNiO_2$, RuO_2 and Pt (see Figure 15b). For $LiNiO_2$, the onset potential was found to be $1.57\,V_{RHE}$, while the potential to reach $10\,mA\,cm^{-2}$ was found to be $1.63\,V_{RHE}$, the Tafel slope was $60\,mV\,dec^{-1}$(see Figure 15c). These results are comparable to those found in other studies for similar material compositions. The $NaNiO_2$ catalyst shows an onset potential of $1.46\,V_{RHE}$ and the potential to reach $10\,mA\,cm^{-2}$ was $1.56\,V_{RHE}$. The Tafel slope for this material was found to be $60\,mV\,dec^{-1}$. Fe-doping leads to the resulting $NaNi_yFe_{1-y}O_2$ showing enhanced OER properties. $NaNi_{0.9}Fe_{0.1}O_2$ has onset potential of $1.40\,V_{RHE}$ and a

ChemElectroChem

Review
doi.org/10.1002/celc.202300761

Chemistry
Europe
European Chemical
Societies Publishing

Figure 15. (a) X-ray diffraction patterns for $NaNi_yFe_{1-y}O_2$ (y = 0.75, 0.80, 0.90, 0.91, 1.00). (b) OER performance of $NaNi_yFe_{1-y}O_2$ (y = 0.75, 0.80, 0.90, 1.00), $LiNiO_2$ Pt and RuO_2. (c)Tafel plots of $NaNi_{0.9}Fe_{0.1}O_2$ measured at different Na times. (d) CP measurement of $NaNi_{0.9}Fe_{0.1}O_2$ and RuO_2, measured for comparison. (e) XPS measurement of $Na_{0.08}Ni_{0.9}Fe_{0.1}O_2$, $NaNi_{0.9}Fe_{0.1}O_2$, $NaNiO_2$ and $LiNiO_2$. Reproduced from Ref.[82] with permission from the Royal Society of Chemistry.

potential of 1.52 V_{RHE} to generate a 10 mA cm^{-2} current density. The Tafel slope of this electrocatalyst is found to be 44 mV dec^{-1}, showing that Fe-doping leads to improved OER kinetics (see Figure 15c). When activities are normalised by the electrochemically active surface area (ECSA) for each catalyst, $NaNi_{0.9}Fe_{0.1}O_2$ shows the highest normalised current density, 2.8 times higher than RuO_2. For the latter commercially available catalyst, the Tafel slope was found to be 73 mV dec^{-1} and the potential to reach 10 mA cm^{-2} was 1.55 V_{RHE}. Chronopotentiometry measurements also show that this catalyst can sustain a10 mA cm^{-2} at 1.52 V_{RHE} for over 70 h, whereas RuO_2, despite operating for up to 20 h in the 1.0 M KOH electrolyte, exhibits a steady increase of potential (see Figure 15d). Such results clearly show how the Fe-doping in the $NaNi_yFe_{1-y}O_2$ family of electro-

catalyst leads to remarkable catalytic properties for the OER compared to benchmark materials such as RuO_2. Ni 2p XPS spectra can be fitted with Ni^{2+} and Ni^{3+} (see Figure 15e) and it was shown that the presence of Na in $NaNiO_2$ forces Ni to adopt its higher oxidation state. When Fe is incorporated, a shift of the Ni peaks to higher binding energies suggests Ni adopts mixed oxidation states of Ni^{3+} and Ni^{4+}, with Fe adopting Fe^{3+} and Fe^{4+} oxidation states. Those higher chemical oxidation states are responsible for the higher adsorption of active species and would significantly improve the charge transfer properties, thus enhancing the rate-determining step as seen by the Tafel slopes. Therefore, the high oxidation states of Ni and Fe are responsible for the enhanced properties of the $NaNi_yFe_{1-y}O_2$ catalysts, particularly for y = 0.9. The

$Na_{0.08}Ni_{0.9}Fe_{0.1}O_2$ was also tested in an unassisted two-electrode solar-driven water splitting device, with NiP, an HER catalyst chosen as an alternative to noble metal HER electrocatalysts, used as the cathode. Such a device showed a solar-to-hydrogen conversion efficiency of 11.2%, while being powered by a lead halide perovskite solar cell. Overall, it has here been shown that the $NaNi_yFe_{1-y}O_2$ double oxides could be good candidates for low-cost electrolysis and shows how interlayer Na promotes the performance towards the OER due to it forcing Ni to higher oxidation states.

4. Layered ruthenium and iridium-based oxides

RuO_2 and IrO_2 are the literature benchmark materials for OER under acidic conditions and there is also a growing interest in alkali metal-containing oxides of these elements. Gao *et al.* showed that the incorporation of Li^+ into amorphous iridium oxide (see Figure 16a) leads to enhanced performance, compared to a crystalline (rutile) analogue suggesting that the Li dopant has a promotional effect both towards the activity and the durability of the catalyst (see Figure 16b). DFT calculations confirmed the OER is thermodynamically more favourable in the amorphous $Li-IrO_x$ than rutile IrO_2 and that the disordered $[IrO_6]$ octahedra are more easily oxidised during the OER although this was not compared to an alkali metal-free amorphous IrO_x.[87]
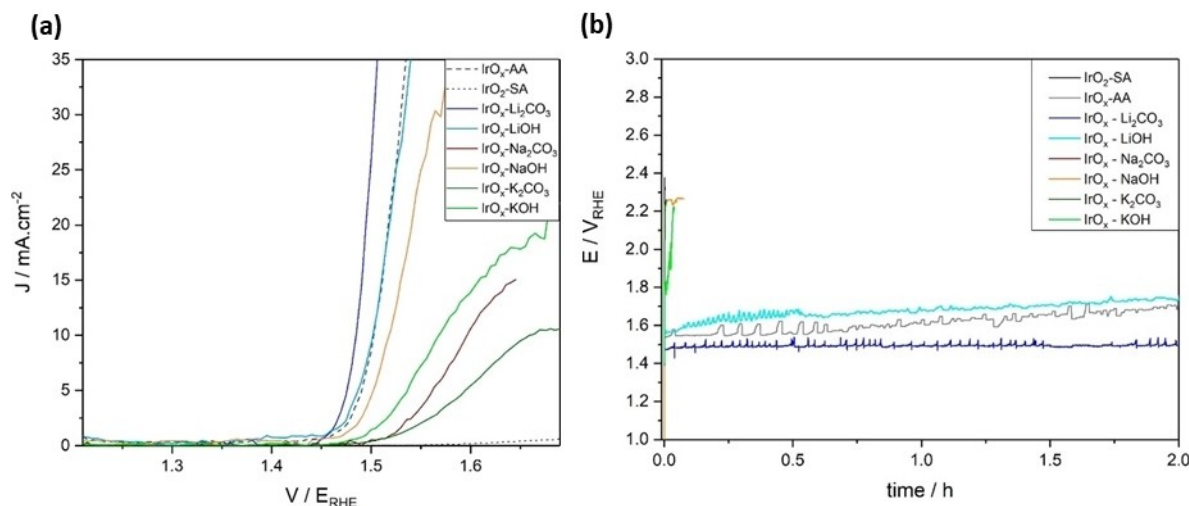
Similar promotional effects were observed in a study by Esquius *et al.*, where the synthesis of amorphous iridium oxohydroxides, $Ir(O)_x(OH)_y$, was carried out *via* a simple hydrothermal method in the presence of different alkali metal salts (Li_2CO_3, $LiOH$, Na_2CO_3, $NaOH$, K_2CO_3, KOH).[32] Such iridium oxohydroxides were tested in 0.1 M $HClO_4$ using a GC, a Pt wire and a SCE as working, counter and reference electrodes, respectively, in a flowing electrochemical cell. It was shown the

alkali metal salt significantly affects the physicochemical properties of the electrocatalyst such as the surface area, the morphology and the concentration of hydroxyl species and Ir(III)/Ir(IV) ratio on the surface, ultimately influencing the catalytic activity and stability of these oxohydroxides. The highest promotional effect of the alkali metal was observed for those $Ir(O)_x(OH)_y$ electrocatalysts prepared with Li-containing salts, *i.e.* lower overpotentials, increased activities and increased stabilities, compared to the commercial amorphous IrO_2 (Premion, Alfa Aesar) (see Figure 17).

Given the effect of lithium and other alkali metals, there has been increasing interest in crystalline alkali metal-layered materials, such as that of lithium iridate, Li_2IrO_3, and lithium ruthenate, Li_2RuO_3. While the latter has been studied in traditional lithium-ion batteries,[88,89] little is known about its electrocatalytic OER performance. The structure for both materials is similar to other two-dimensional transition metal electrocatalysts discussed above:$[RuO_6]$ and $[IrO_6]$ octahedra propagate in two dimensions, forming metal-oxo layers, while Li^+ and Na^+ cations occupy interlayer sites resulting in monoclinic crystalline structures.[90–93] For instance, both Li_2IrO_3 and Li_2RuO_3 have been found to adopt a $C2/m$ monoclinic space group. Different interlayer cation sizes lead to variations in the *d*-spacing between metal-oxo sheets. As an example, when Li^+ is replaced by Na^+ cations, interlayer distances of ~4.8 and ~5.3 Å are found for Li_2IrO_3 and Na_2IrO_3, respectively.[90] Yang *et al.* investigated the properties of $\alpha-Li_2IrO_3$ featuring a monoclinic structure with $C2/m$ space group and interlayer Li sites,[90] which forms a hydrated birnessite phase (space group $R\bar{3}m$), $Li_xK_{0.3}IrO_3·0.7H_2O$, when being cycled in K-containing alkaline electrolyte (KOH, GC RDE, KCl-saturated Ag/AgCl and Pt wire as working, counter and reference electrode, respectively) due to delithiation and the insertion of potassium ions from the electrolyte (see Figure 18a and 18b). Such a phase exhibits a five-fold increase of activity towards OER compared to $\alpha-Li_2IrO_3$
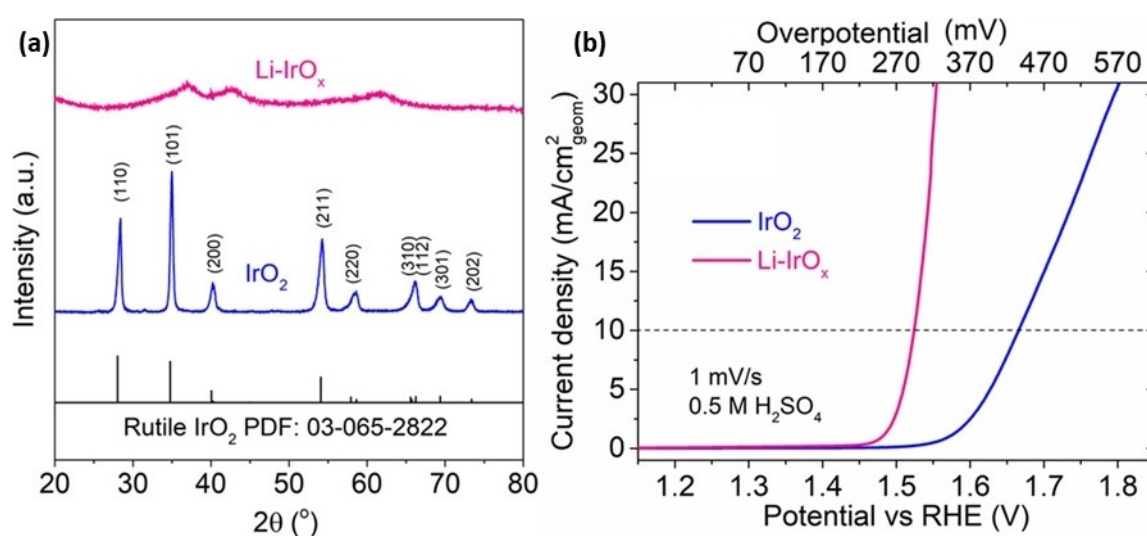
Figure 16. (a) Powder X-ray diffraction pattern of amorphous $Li-IrO_x$ and $r-IrO_2$, with a simulated $r-IrO_2$ pattern included for reference and (b) LSV curves for amorphous $Li-IrO_x$ and $r-IrO_2$ in acidic conditions (0.5 M H_2SO_4) with the latter showing enhanced activity towards the OER. Adapted with permission from *J. Am. Chem. Soc. 2019, 141, 7, 3014–3023*. Copyright 2019 American Chemical Society.
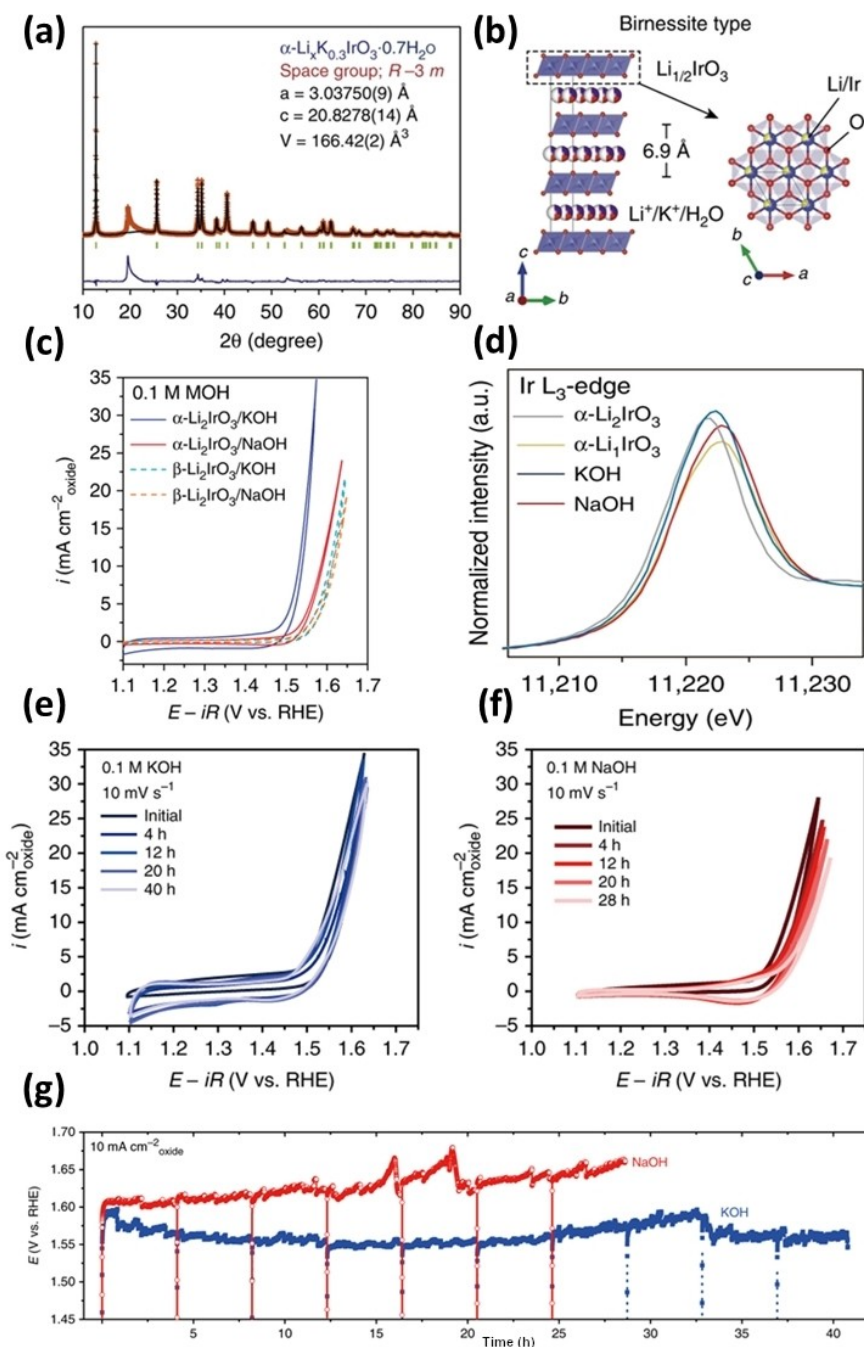
ChemElectroChem

Review
doi.org/10.1002/celc.202300761

Chemistry Europe
European Chemical
Societies Publishing

Figure 17. (a) LSV curves of commercial IrO_2 standards and hydrothermally prepared IrO_x catalysts (1.2 V_{RHE} to 1.7 V_{RHE} at 5 mV s^{-1}) and (b) catalyst stability assessment *via* chronopotentiometry (2 h at 10 mA cm^{-2}). Adapted with permission from *ACS Appl. Energy Mater.* 2020, 3, 1, 800–809. Copyright 2019 American Chemical Society.

in (see Figure 18c).[94] XAS measurements of this material at the Ir L$_3$-edge show a shift in the white line observed for α-Li$_1$IrO$_3$ compared to α-Li$_2$IrO$_3$, indicating an increase of oxidation state from Ir^{4+} to Ir^{5+} during delithiation (see Figure 18d).[95,96] Upon exposure of α-Li$_1$IrO$_3$ to 1 M KOH, the insertion of potassium into the iridium oxide and the formation of the birnessite phase is accompanied by the reduction of Ir to an average oxidation state between 5 + (α-Li$_1$IrO$_3$) and 4 + (α-Li$_2$IrO$_3$). Hence, upon the reaction of α-Li$_1$IrO$_3$ with the electrolyte, the catalyst is reduced. This process is selective to the nature of the cation since no reduction of Ir (*i.e.*, no shift of the white line) was detected by XAS after soaking α-Li$_1$IrO$_3$ in NaOH. Such a transition was not observed for catalytic cycles in NaOH, despite the smaller ionic radius of Na$^+$ (1.02 *vs* 1.38 Å for K$^+$) which would suggest an easier insertion in the interlayer sites. Such a transition was also not observed for the β-Li$_2$IrO$_3$ polymorph, which features an orthorhombic *Fddd* space group.[97] A combination of energy-dispersive X-ray spectroscopy (EDX), XRD, solid-state nuclear magnetic resonance (ssNMR) and thermogravimetric analysis (TGA) allowed the determination of the composition of the electrocatalyst formed in the presence of KOH, Li$_x$K$_{0.3}$IrO$_3 \cdot$0.7H$_2$O ($x \leq 1$). Once formed, this catalyst shows similar catalytic behaviour both in NaOH and KOH electrolyte, as shown by CV and CP curves (see Figure 18e, 18f and 18e). This highlights the role the crystalline structure might play in triggering phase transitions and indirectly enhancing the OER electrocatalytic properties. The transformation to α-Li$_1$IrO$_3$ electrocatalyst at pH 13 occurs at ~1.23 V_{RHE} when employing α-Li$_2$IrO$_3$ as the starting electrocatalyst, as shown by an irreversible oxidation peak during the first cycle, and exhibits remarkable OER activity thereafter, with an overpotential of 290 mV at 10 mA cm^{-2}.

The synthesis of iridate and ruthenate materials remains challenging and often requires high temperatures and extended times, *e.g.* Li$_2$IrO$_3$ can be synthesised at 1080 $^\circ$C for 30 h.[98] Similarly, Li$_2$RuO$_3$ can be obtained *via* conventional solid-state reactions at ~900 $^\circ$C for 12 h.[99] Pearce *et al.* have

recently demonstrated that the deintercalation of Li cations from β-Li$_2$IrO$_3$ leads to the formation of β-Li$_1$IrO$_3$, β-Li$_{0.5}$IrO$_3$ and β-IrO$_3$ (see Figure 19a), the latter being an unstable phase that can only be stabilised in non-aqueous solvents as an intermediate in Ir-based catalysts due to its high valence Ir.[100] Deintercalation of Li was achieved by loading β-Li$_2$IrO$_3$ as a cathode material in a Li-ion battery and discharging at defined potentials, *i.e.* 4.1, 4.6 and 4.8 $V_{Li\backslash Li^+}$. Furthermore, a hydrated β-H$_2$IrO$_3$ was prepared by hydrothermal ion exchange in a 1 M H$_2$SO$_4$ solution at 120 $^\circ$C for 36 h, structural refinements of synchrotron XRD and neutron diffraction data indicate this hydrated compound adopts an orthorhombic structure of *Fddd* space group. When exposed to 1 M H$_2$SO$_4$, β-IrO$_3$ and β-Li$_{0.5}$IrO$_3$ are found to chemically evolve oxygen non catalytically, while β-LiIrO$_x$ does not evolve oxygen under the same conditions (see Figure 19b). Such a phenomenon was ascribed to the redox potential of β-IrO$_3$ and β-Li$_{0.5}$IrO$_3$, *i.e.* 4.55 and 4.4 $V_{Li\backslash Li^+}$, being above the reversible potential for water oxidation at pH = 0 (4.23 $V_{Li\backslash Li^+}$). On the contrary, β-LiIrO$_3$ has a redox potential of 3.4 $V_{Li\backslash Li^+}$ and cannot therefore oxidise water spontaneously. Thus, β-IrO$_3$ and β-Li$_{0.5}$IrO$_3$ are unstable in acidic electrolyte, act as oxidizing reactants and the amount of oxygen produced depends on the oxidation state and the concentration of the Ir sites. Increasing amounts of Ir leached from the active materials during acid soaking for higher valence iridium compounds suggesting the more electrophilic O^{n-} species found *via* XAS and XPS measurements were responsible for higher activity and lower stability of the catalysts during OER. When studying the protonated β-H$_2$IrO$_3$ phase, the protons can be continuously exchanged between this electrocatalyst and the acidic electrolyte during the OER, therefore regenerating the catalyst and limiting the dissolution. This indicates that the design of electrocatalysts with reversible proton exchange capabilities may be pivotal in the fabrication of stable and active catalysts in acidic electrolytes.
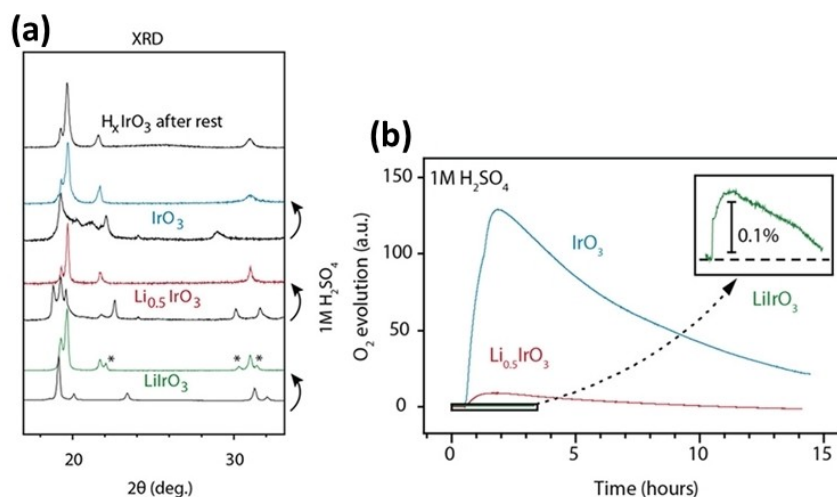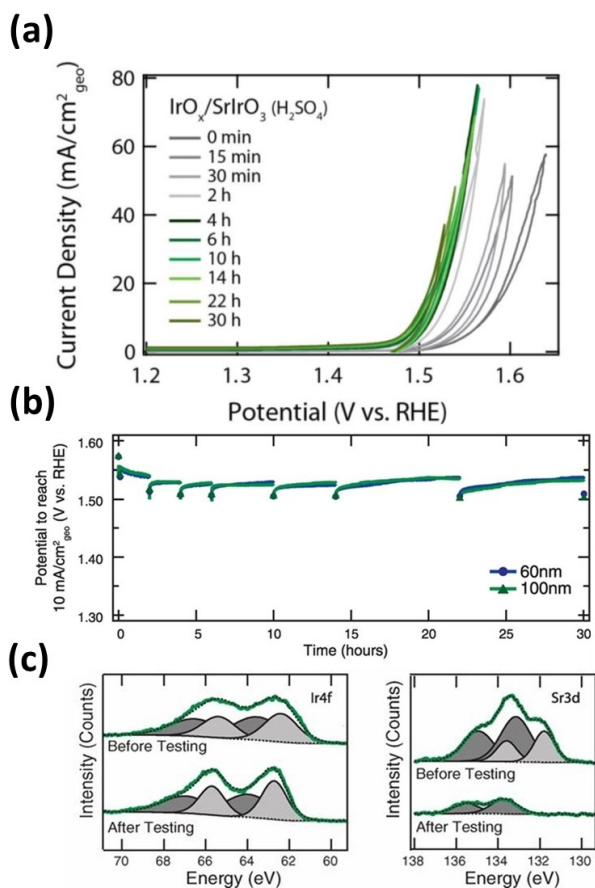
ChemElectroChem

Review
doi.org/10.1002/celc.202300761

Chemistry Europe
European Chemical
Societies Publishing

Figure 18. (a) Powder X-ray diffraction pattern and Rietveld refinement for the birnessite phase, $Li_xK_{0.3}IrO_3 \cdot 0.7H_2O$. (b) Representation of the layered structure of the birnessite phase, $Li_xK_{0.3}IrO_3 \cdot 0.7H_2O$. (c) X-ray absorption comparison of α-Li_2IrO_3, α-Li_1IrO_3 and after cycling of Ir in KOH and NaOH. (d) CV curves of the layered α-Li_2IrO_3 phase compared to the 3D β-Li_2IrO_3 polymorph in 0.1 M KOH and NaOH aqueous solutions. CV curves of α-Li_1IrO_3 at definite times in (d) 0.1 M KOH and (e) 0.1 M NaOH. (f) CP measurements for α-Li_1IrO_3 in 0.1 M KOH and 0.1 M NaOH. Adapted from ref.[94] with permission from Nature Communications.

In 2016, Seitz *et al.* reported a mixed $IrO_2/SrIrO_3$ catalyst, obtained *in situ* from thin films of $SrIrO_3$, epitaxially grown on $SrTiO_3$, due to the leaching of strontium from their surface.[101] Such electrocatalysts were found to be stable in the acidic electrolyte (0.5 M H_2SO_4, Pt wire as counter electrode, K_2SO_4-saturated $Hg/HgSO_4$ as reference electrode and Cu wires used as contacts to the perimeter of the film) and to outperform commercially available IrO_2 catalysts (see Figure 20a). It was found from CV experiments that the electrocatalyst requires a

340 mV overpotential to reach 10 mA cm^{-2} and that after 10 min this drops to 320 mV to reach the same current density. Complimentary CP measurements have shown that the electrocatalyst is stable for up to 30 h and requires even lower overpotentials, *i.e.* 270 and 290 mV, to hold 10 mA cm^{-2} current density during the first 2 h of the experiment (see Figure 20b). For comparison purposes, a IrO_2 (110) film on TiO_2 was also synthesised but underperformed by two orders of magnitudes when compared to the $IrO_x/SrIrO_3$ catalyst. DFT calculations

ChemElectroChem

Review
doi.org/10.1002/celc.202300761

Chemistry Europe
European Chemical
Societies Publishing

Figure 19. (a) XRD patterns for LiIrO₃, Li₀.₅IrO₃, IrO₃ and HₓIrO₃ and (b) O₂ evolution upon exposure of LiIrO₃, Li₀.₅IrO₃, IrO₃ to H₂SO₄. Adapted with permission from *Chem. Mater.* 2019, 31, 15, 5845–5855. Copyright 2019 American Chemical Society.
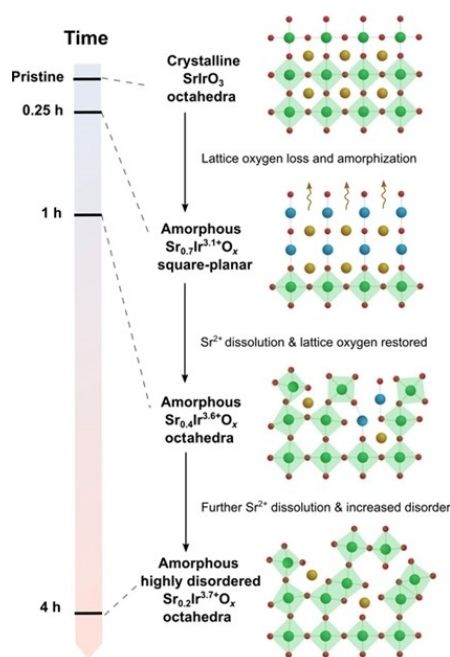

Figure 20. (a) Geometric area-normalised CV curves current density of a 100 nm IrOₓ/SrIrO₃ film at several times during 30 hours of electrochemical stability testing. (b) Potential required to reach 10 mA/cm²$_{geo}$ for IrOₓ/SrIrO₃ films during 30 hours of electrochemical testing. Markers indicate CV measurements and lines indicate CP holds. (c) XPS of the Ir4f and Sr3d peaks for a 100 nm SrIrO3 before and after 30 minutes of OER testing. Adapted from Ref.[81]

have suggested that SrIrO₃ activity towards OER is enhanced due to Sr leaching into the electrolyte and that the formation of

IrO₃ and anatase IrO₂ sites could cause such an enhancement, ultimately confirming that surface strontium deficiencies can increase the activity of SrIrO₃. Such results from simulations have been confirmed *via* XPS measurements of the Ir 4f and Sr 3d orbitals during OER (see Figure 20c). It was shown that the Sr 3d signal decreases during OER by 25–28% in 30 min, consistent with further results obtained *via* ICP-OES showing a similar Sr content leaching in solution during 30 min.

In 2021, Wan *et al.* specifically investigated the interfacial transformation of highly crystalline and homogenous epitaxially-grown SrIrO₃ during the catalytic process and have found that SrIrO₃ undergoes an amorphisation process triggered by lattice oxygen activation, which increases the concentration of oxygen vacancies and allows the diffusion of Sr²⁺ and the reorganisation of O²⁻ in the structure, while progressively disordering the [IrO₆] octahedra framework (see Figure 21).[102] The highly amorphous layer that forms on top of the SrIrO₃ crystalline bulk is ~2.4 nm thick. These results on SrIrO₃ as a model catalyst for OER show how applied potentials promote the formation of amorphous layers and how such an interfacial transition is activated by the coupled diffusion of ionic species.

Recently, Esquius *et al.* have shown that nanocrystalline Li-intercalated iridium oxide, Li-IrOₓ, can be synthesised *via* a facile synthesis method starting from iridium oxyhydroxides previously discussed.[28] It has been found that when annealing at ~500 °C for as little as 3 h under static air the residual lithium carbonate following synthesis leads to the formation of the nanocrystalline layered material and suppresses the formation of r-IrO₂ (T > 425 °C) (see Figure 22a). This demonstrates that layered materials can be fabricated under milder conditions than those typically reported by using amorphous IrOₓ rather than Ir black or rutile IrO₂ as the Ir source.[28,91] The principal XRD reflection at ~18° suggests the interlayer spacing of 4.8 Å between the Ir-oxo sheets, consistent with the literature.[36,48] XPS surface analysis of the Ir 4f energy levels revealed the presence of features at 62.3 eV typical of this Li-IrOₓ material and found in other amorphous Ir(O)ₓ(OH)ᵧ previously

ChemElectroChem

Review
doi.org/10.1002/celc.202300761

Chemistry
Europe
European Chemical
Societies Publishing

Figure 21. Postulated crystalline-to-amorphous transformation pathway in $SrIrO_3$. The oxygen loss from the lattice oxygen is the activation step for the transformation from crystalline $SrIrO_3$ to Sr-doped amorphous IrO_x. The proposed square-planar geometry of the latter has a weak network, allowing further dissolution of Sr and leading to the square-planar structure collapsing into a disordered Ir(III)/Ir(IV) mixture. Adapted from Wan *et al.*, *Sci. Adv.* 2021; 7:eabc7323.

studied.[103,104] Further XPS studies show a high Ir(III)/Ir(IV) surface ratio of this Li-doped layered IrO_x, ascribed to a higher concentration of chemisorbed H_2O and –OH surface terminations, similar to amorphous IrO_x (see Figure 22b). NEXAFS measurements of the O K-edges were carried out to probe the surface oxygen species in Li-IrO_x and have indicated three absorption features which were directly compared to commercially available r-IrO_2 and the amorphous analogue for reference (see Figure 22c). Two of these features were attributed to transitions of the O 1s core electrons into hybridised O 2p-Ir 5d states, whereas the third absorption peak found at higher energies was attributed to similar transitions into the O 2p-Ir 6s-p hybridised states. Due to the lower intensity of the first of these three features, Li-IrO_x has a lower degree of hybridisation between Ir 5d and O2p orbitals than IrO_2. In r-IrO_2, a shorter Ir–Ir distance in the direction perpendicular to the edges shared by the octahedra is responsible for distortions of the [IrO_6] octahedra. In Li-IrO_x, such resonance is found at higher energies, indicating longer Ir–O bonds and the distortion typical of r-IrO_2 is not observed. As opposed to many of the previous studies so far, this layered electrocatalyst has here been studied in acidic conditions (0.1 M $HClO_4$, GC as the working electrode, Pt-wire as counter electrode and SCE as the reference electrode) to assess its activity and stability when compared to the commercially available benchmark compounds, r-IrO_2 and IrO_x, widely investigated for their applications in acidic electrolytes. LSV curves have shown Li-IrO_x remarkably exhibits comparable activity to commercially available amorphous IrO_x (see Figure 22d) despite

being treated at 500 °C. In particular, Li-IrO_x reached a current density of 10 mA cm^{-2} at an overpotential of 290 mV, lower than that of r-IrO_2 (390 mV), albeit higher than that of IrO_x (270 mV). This layered Li-IrO_x does not seem to undergo the same fast degradation which severely limits amorphous IrO_x, but rather exhibits a long-term stability of up to 75 h.

Sun *et al.* reported a $K_{0.25}IrO_2$ electrocatalyst,[105] which had previously been shown to adopt a hollandite-type crystal structure, with a monoclinic unit cell and $I2/m$ space group.[106] It should be pointed out that, while still featuring both edge-sharing and K-connected [IrO_6] octahedra, this compound does not feature a layered structure like the materials discussed above. Nonetheless, we feel it is still worth mentioning that the presence of K^+ cations in such a material yields an electrocatalyst exhibiting excellent OER activity compared to IrO_2. In particular, $K_{0.25}IrO_2$ shows a higher catalytic activity than IrO_2 and exhibits a small overpotential of 350 mV at 10 mA cm^{-2} when tested in 0.1 M $HClO_4$ using a Pt-foil and a SCE as counter and reference electrodes, respectively (see Figure 23a). By contrast, IrO_2 only reaches 3.15 mA cm^{-2} when a similar overpotential is applied. DFT simulations have confirmed the theoretical overpotential of $K_{0.25}IrO_2$ is lower compared to that of IrO_2, *i.e.* 0.5 *vs* 0.61 V. Chronoamperometric tests carried out at 1.68V_{SCE} for close to 5 hours show that the current density slowly declines for $K_{0.25}IrO_2$ and IrO_2, ascribed to the formation of oxygen bubbles, and confirmed by post-CA CV curves showing a close overlap with pre-CA measurements (see Figure 23b and 23c). XPS data revealed that Ir 4f peaks shift to lower binding energies compared to IrO_2, suggesting Ir species have a lower valence. O 1s XPS spectra also show that the binding energy of lattice oxygen in $K_{0.25}IrO_2$, centred at 529.54 eV, is lower than that found for IrO_2 (529.76 eV), ascribed mainly to the different structures of the two electrocatalysts. XANES measurements of the Ir-L_3 edge suggest a higher electron density of the Ir sites in $K_{0.25}IrO_2$ compared to IrO_2 due to a significantly lower intensity of the white line, indicating more 5d states are occupied in the former electrolyte. Indeed, the intensity of the white line is related to the number of electron transitions from 2p orbitals of the ligand to the 5d orbitals of the metal. Thus, a less intense white line indicates more saturation of the 5d states. A lower adsorption energy of the Ir-L_3 edge in $K_{0.25}IrO_2$ compared to IrO_2 confirmed the lower valence state adopted by Ir sites in $K_{0.25}IrO_2$.

Zhu *et al.* have recently investigated the properties of two layered phases, $K_{0.3}IrO_2 \cdot xH_2O$ and $Rb_{0.3}IrO_2 \cdot xH_2O$, prepared *via* a facile hydrothermal method.[107] A combination of XRD and HRTEM measurements show these two materials adopt a layered structure in the hexagonal $R\bar{3}m$ space group with the distance between layers of IrO_2 of 6.9 and 7.0 Å for $K_{0.3}IrO_2 \cdot xH_2O$ and $Rb_{0.3}IrO_2 \cdot xH_2O$, respectively, and showing a significant degree of [IrO_6] octahedra distortions, particularly when Rb^+ cations occupy the interlayer sites (see Figure 24a, 24b, 24c and 24d). Furthermore, it was concluded that the stacking of the IrO_2 layers was of the 3R-type, *i.e.* layers stack in a staggered ABC sequence. It was shown *via* EDX measurements that the exchange of hydrogen ions in HCl solution with K^+ or Rb^+ in the interlayer sites leads to the formation of two so-called 3R-
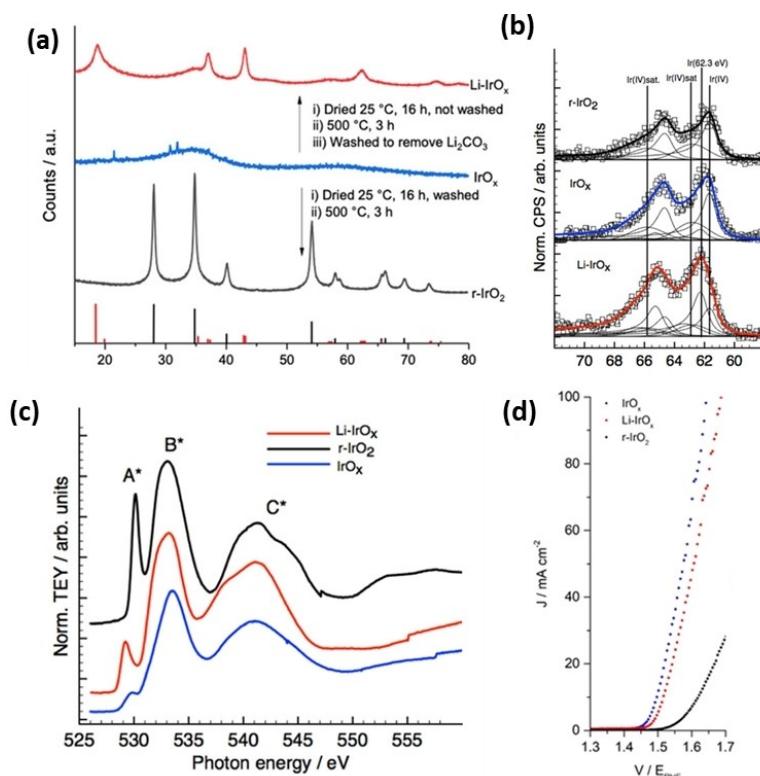
Figure 22. (a) XRD patterns of samples prepared from IrO$_x$. Black reference pattern rutile IrO$_2$ [ICSD-56009], red reference pattern Li$_2$IrO$_3$ [ICSD-246025]. (b) Fitted Ir 4f XPS spectra measured in UHV and at an electron kinetic energy (KE) of 200 eV (c) Total electron Yield (TEY) O K-edge NEXAFS spectra measured for IrO$_x$, Li-IrO$_x$, and r-IrO$_2$ d) LSV measurements of IrO$_x$, Li-IrO$_x$ and r-IrO$_2$ (LSV, 1.2–1.7 V$_{RHE}$, 5 mV s^{-1} Adapted with permission from *J. Am. Chem. Soc.* 2023, 145, 11, 6398–6409. Copyright 2023 American Chemical Society.
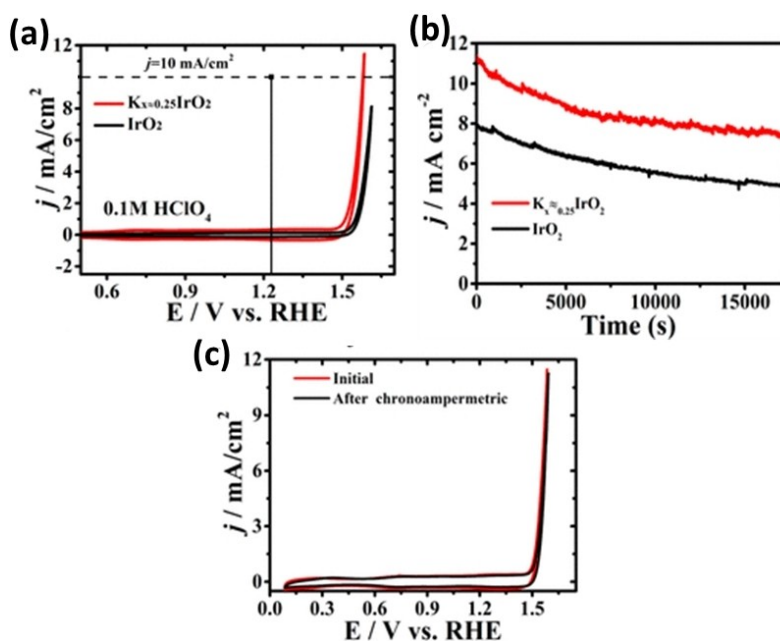
Figure 23. (a) Polarization curves with *iR* correction for OER of K$_{0.25}$IrO$_2$ and IrO$_2$ (solution resistance 33 Ω), with vertical lines indicating the theoretical potential for OER, the horizontal dash indicated the *j* = 10 mA cm^{-2}. (b) CA measurements for K$_{0.25}$IrO$_2$ and IrO$_2$ at 1.68 V$_{RHE}$ constant. (c) Polarization curves for K$_{0.25}$IrO$_2$ before and after CA experiments. Adapted with permission from *ACS Appl. Mater. Interfaces* 2016, 8, 1, 820–826. Copyright 2015 American Chemical Society.

IrO$_2$ compounds, *i.e.* 3R-IrO$_2$-K and 3R-IrO$_2$-Rb, where K and Rb here denote the precursor from which they have been

obtained. EDX measurements confirm that K and Rb are undetectable after hydrogen ion exchange, indicating this
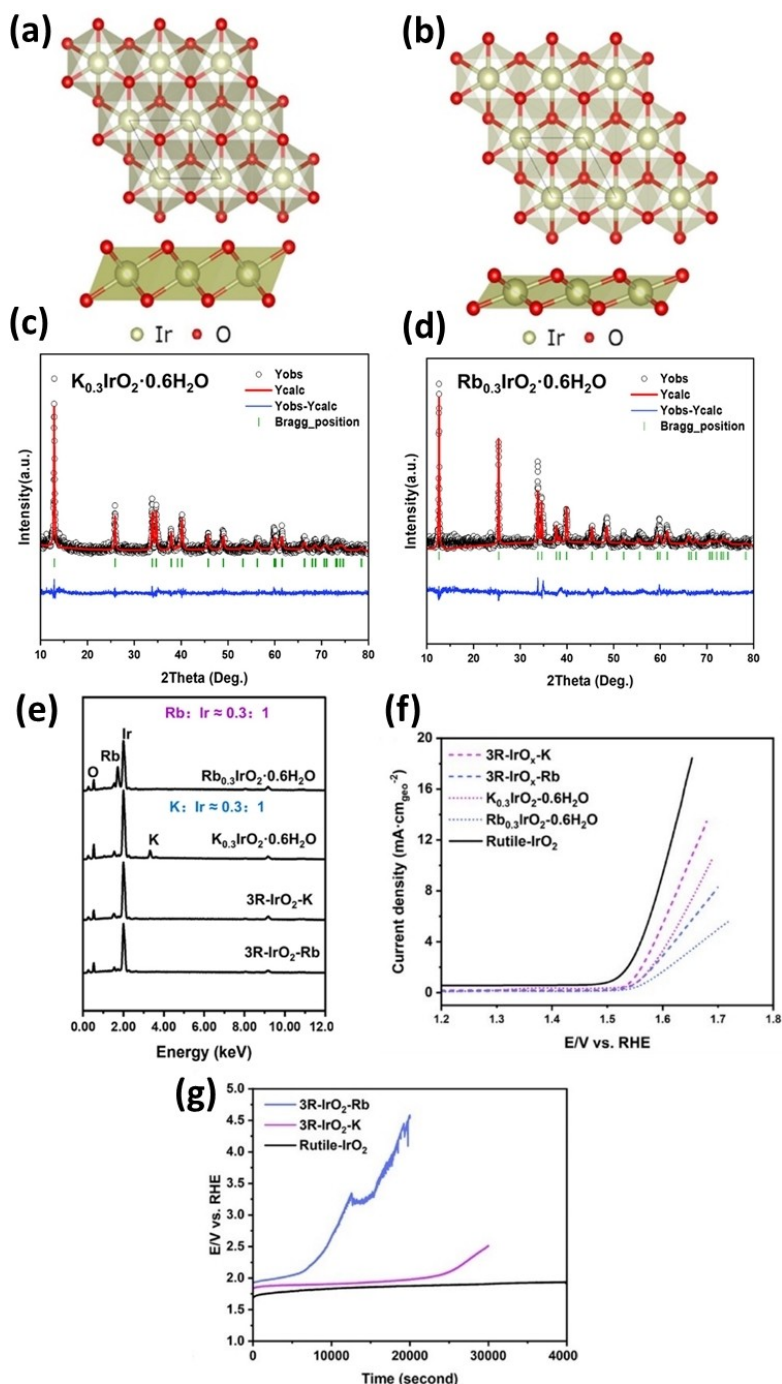
Figure 24. Layered structure of (a) $K_{0.3}IrO_2 \cdot 0.6H_2O$ and (b) $Rb_{0.3}IrO_2 \cdot 0.6H_2O$, showing a significant degree of [IrO_6] octahedra distortions. X-ray diffraction patterns and Rietveld refinements of (c) $K_{0.3}IrO_2 \cdot 0.6H_2O$ and (d) $Rb_{0.3}IrO_2 \cdot 0.6H_2O$. (e) EDX measurements $K_{0.3}IrO_2 \cdot xH_2O$, $Rb_{0.3}IrO_2 \cdot xH_2O$, $3R$-IrO_2-K, and $3R$-IrO_2-Rb f LSV measurements of $3R$-IrO_2-K, $3R$-IrO_2-Rb, $K_{0.3}IrO_2 \cdot 0.6H_2O$, $Rb_{0.3}IrO_2 \cdot 0.6H_2O$, and rutile IrO_2. (g) Stability measurements obtained *via* chronopotentiometry for $3R$-IrO_2-K, $3R$-IrO_2-Rb, and rutile IrO_2. Adapted with permission from *ACS Appl. Energy Mater.* 2023, 6, 9, 4757–4765. Copyright 2023 American Chemical Society.

process completely removes these cations from the structure (see Figure 22e). XRD patterns have shown that after ion exchange, reflections at ~20°, arising from the layers, shift to higher angles, suggesting the interlayer distance is reduced after the removal of K^+ and Rb^+ cations. Indeed, these two structures exhibited the same interlayer spacing of ~4.64 Å, although the [IrO_6] octahedra distortions remained unchanged. HRTEM measurements of $3R$-IrO_2-K and $3R$-IrO_2-Rb confirmed

the hexagonal structure is maintained, with these two compounds sharing identical electron diffraction patterns. Interestingly, it has been shown that these electrocatalysts feature significantly different OER properties when tested in 0.1 M $HClO_4$ using a three-electrode setup with a Pt-foil and a SCE as counter and reference electrodes, respectively. For instance, the order of the OER activity is $Rb_{0.3}IrO_2 \cdot 0.6H_2O < K_{0.3}IrO_2 \cdot 0.6H_2O < 3R$-$IrO_2$-Rb $< 3R$-IrO_2-K $< IrO_2$ (see Figure 22f). In addition to

this, these catalysts showed worse stability than IrO_2, with 3R-IrO_2-K and 3R-IrO_2-Rb featuring the lowest stability among the studied electrocatalysts (see Figure 22g). XPS analysis showed $K_{0.3}IrO_2 \cdot 0.6H_2O$ and $Rb_{0.3}IrO_2 0.6H_2O$ feature mixed valence Ir^{3+} and Ir^{4+} states, whereas the two 3R-IrO_2 compounds showed a significantly lower concentration of Ir^{3+}. The adsorption of OH species by the catalyst leads to a reduction of the Ir species in the electrocatalysts during the OER. Thus, the high presence of reduced Ir^{3+} is also an indication of lower OH group concentrations in the two 3R-IrO_2 structures during the OER. XANES at the O—K edge indicates the Ir—O bond covalency hybridisation of the Ir 5d and O 2p orbital is highest in the 3R-IrO_2 structures due to increased d-holes. Such d-holes are inversely proportional to the concentration of oxygen vacancies. Therefore, the OER activities observed are directly correlated to the concentration of d-holes and the degree of orbital hybridisation, whereas all of these factors are inversely correlated to the concentration of oxygen vacancies. In other words, it has been concluded that the catalytic properties of the studied electrocatalysts deteriorate with higher lattice distortions and the resulting oxygen vacancies are found to be responsible for the hindered Ir 5d – O 2p hybridisation.

5. Summary and Perspective

In this review, we have summarised a selection of the recently reported alkali metal-layered electrocatalysts for the OER evolution reaction, focusing primarily on Li^+ containing materials. Such electrocatalysts are typically transition metal-based compounds, (Co, Mn, Cr, Ni and Ir) and have been tested in

alkaline conditions. First, the inclusion of Li^+ as an interlayer species often yields compounds with higher performances towards OER than simple metal oxides (see Table 1 for a summary of available overpotentials measured at the onset of the OER and at the benchmark current of 10 mA cm^{-2}). Furthermore, the process of delithiation seems to play a key role in influencing electrocatalytic properties towards the OER, with compounds such as $Li_{0.5}CoO_2$ derived from Li_2CoO_2 and Co-based lithium-containing oxides demonstrating significantly enhanced performance following lithium deintercalation. In many instances, this process leads to an amorphization of the surface structure and enhanced electrochemical surface areas. These observations suggested that a controlled delithiation process in organic electrolytes allows some degree of structural and compositional tuning which is not possible on anodic delithiation in aqueous electrolytes.

The introduction of dopants, including Fe, Al, Mn, has in more than one case significantly improved the catalytic activity of materials, as seen in the $LiNi_{1-x}M_xO_2$ compounds, with Fe doping proving particularly effective in improving OER performance, showing a synergistic effect between different metal centres to further improve the performance of this layered electrocatalysts. In addition to interlayer Li cations, the inclusion of other alkali metals in layered oxides reveals an interesting and positive effect, as seen in $NaCoO_2$, where the inclusion of interlayer Na^+ leads to enhanced OER properties. Importantly, this indicates that the fabrication of alkali-metal layered metal oxides is not constrained by the use of lithium and that other metals may have a greater enhancing effect.

The ever-growing interest in acidic electrolytes – due to the higher mobility of H^+ ions – has led to investigations of

Table 1. Available values of (i) onset potentials and (ii) potentials required to achieve 10 mA cm^{-2}, the benchmark current for the reviewed electrocatalysts.

Material	Onset η (mV)	η @ 10 mA cm^{-2} (mV)	Reference
$LiCoO_2$	1.6	–	[63]
$LiCoO_2$	1.59	–	[64]
$Li_{0.5}CoO_2$	1.52	–	[64]
$LiCo_{0.33}Ni_{0.33}Fe_{0.33}O_2$	1.47	1.52	[64]
$LiCo_{0.8}Fe_{0.2}O_2$	1.49	–	[75]
$Na_{0.36}CoO_2$	–	1.64	[79]
$NaCo_{0.75}Fe_{0.25}O_2$	–	1.54	[108]
RuO_2	–	1.58	[108]
$Li_{0.6}Cr_{0.9}Fe_{0.1}O_2$	–	1.54	[109]
$LiNiO_2$	1.57	1.63	[108]
$NaNiO2$	1.46	1.56	[108]
$NaNi_{0.9}Fe_{0.1}O_2$	1.40	1.52	[108]
α-Li_2IrO_3	–	1.52	[94]
β-H_2IrO_3	–	1.58	[100]
$SrIrO_3$ (thin film)	–	1.57-1.55	[101]
Li-IrO_x	–	1.52	[28]
IrO_x	–	1.5	[28]
IrO_2	–	1.62	[28]
$K_{0.25}IrO_2$	–	1.58	[28]

electrocatalysts able to withstand such harsh conditions, *e.g.* IrO$_2$ and Li-layered iridium oxides. Iridium-based electrocatalysts are considered benchmark materials for acidic OER. Stability and long-term performance are the most desirable characteristics for such materials in industrial applications, with efforts, therefore, focusing on achieving durability in harsh acidic and oxidative conditions. Incorporating alkali metals into iridium oxide-based electrocatalysts is an effective strategy to break the high activity–low stability relationship observed in many catalysts and it has been shown that layered electrocatalysts, such as Li$_2$IrO$_3$, Li-IrO$_x$, and K$_{0.25}$IrO$_2$, have improved performances in acidic conditions were most electrocatalyst fail to reach satisfactory performances. The influence of lattice distortions induced by alkali metals, such as Rb and K, on catalytic properties has also been explored, revealing that higher lattice distortions and resulting oxygen vacancies can hinder Ir 5d–2p O hybridization, leading to deteriorated catalytic performance. Overall, these findings contribute valuable insights into the multiple factors influencing the design and performance of electrocatalysts for OER applications.

In conclusion, the inclusion of alkali metal-layered electrocatalysts for the OER in alkaline and acidic conditions might indeed pave the way to achieving better electrocatalysts. The diverse landscape of materials with promising electrocatalytic properties also suggests alternatives to the more expensive iridium-based materials could be achieved, significantly reducing the production- and operational-related costs of such materials using facile synthetic methods and their extended durability, which, in an industrial setting, is of the utmost importance even at the expenses of high current densities. In addition to this, the fabrication of alloys might be promising, as revealed by the synergistic effects between the different transition metals. However, it has also been shown that intricate relationships between the composition, structure – including structural transformations – morphology and electronic properties play a key role in determining the OER performance and it is often not clear what the underlying mechanisms of the OER are for each catalyst. In this respect, physicochemical characterisations, particularly, when conducted *in situ* and in *operando* conditions, play a vital role in understanding the underlying mechanisms, and computer simulations can indeed aid in such a feat. Future research in this field holds the potential to uncover novel materials and design principles, bringing us closer to sustainable and high-performance electrocatalysis for the transition to a net-zero emission, hydrogen-driven economy.

Acknowledgements

Conflict of Interests

The authors declare no conflict of interest.

[1] I. P. Jain, C. Lal, A. Jain, *Int. J. Hydrogen Energy* **2010**, *35*, 5133–5144.
[2] P. J. Megía, A. J. Vizcaíno, J. A. Calles, A. Carrero, *Energy Fuels* **2021**, *35*, 16403–16415.
[3] H. C. Lau, in *Day 1 Tue, March 23, 2021*, IPTC, **2021**.
[4] M. Katebah, M. Al-Rawashdeh, P. Linke, *Clean Eng Technol* **2022**, *10*, 100552.
[5] M. Plevová, J. Hnát, K. Bouzek, *J. Power Sources* **2021**, *507*, 230072.
[6] D. A. Corrigan, *J. Electrochem. Soc.* **1987**, *134*, 377–384.
[7] G. Młynarek, M. Paszkiewicz, A. Radniecka, *J. Appl. Electrochem.* **1984**, *14*, 145–149.
[8] J. W. Schultze, S. Mohr, M. M. Lohrengel, *J. Electroanal. Chem. Interfacial Electrochem.* **1983**, *154*, 57–68.
[9] S. E. S. El Wakkad, A. Hickling, *Trans. Faraday Soc.* **1950**, *46*, 820–824.
[10] M. Morita, C. Iwakura, H. Tamura, *Electrochim. Acta* **1977**, *22*, 325–328.
[11] H. Bode, K. Dehmelt, J. Witte, *Electrochim. Acta* **1966**, *11*, 1079–1087.
[12] S. Trasatti, *Electrochim. Acta* **1984**, *29*, 1503–1512.
[13] A. Vojvodic, J. K. Nørskov, *Science* **2011**, *334*, 1355–1356.
[14] J. Suntivich, K. J. May, H. A. Gasteiger, J. B. Goodenough, Y. Shao-Horn, *Science* **2011**, *334*, 1383–1385.
[15] I. C. Man, H. Su, F. Calle-Vallejo, H. A. Hansen, J. I. Martínez, N. G. Inoglu, J. Kitchin, T. F. Jaramillo, J. K. Nørskov, J. Rossmeisl, *ChemCatChem* **2011**, *3*, 1159–1165.
[16] J. Pérez-Ramírez, N. López, *Nat. Catal.* **2019**, *2*, 971–976.
[17] J. Song, C. Wei, Z.-F. Huang, C. Liu, L. Zeng, X. Wang, Z. J. Xu, *Chem. Soc. Rev.* **2020**, *49*, 2196–2214.
[18] S. Cherevko, A. R. Zeradjanin, A. A. Topalov, N. Kulyk, I. Katsounaros, K. J. J. Mayrhofer, *ChemCatChem* **2014**, *6*, 2219–2223.
[19] K. Schweinar, B. Gault, I. Mouton, O. Kasian, *J. Phys. Chem. Lett.* **2020**, *11*, 5008–5014.
[20] T. Binninger, R. Mohamed, K. Waltar, E. Fabbri, P. Levecque, R. Kötz, T. J. Schmidt, *Sci. Rep.* **2015**, *5*, 12167.
[21] O. Kasian, J. Grote, S. Geiger, S. Cherevko, K. J. J. Mayrhofer, *Angew. Chem. Int. Ed.* **2018**, *57*, 2488–2491.
[22] S. Fierro, T. Nagel, H. Baltruschat, C. Comninellis, *Electrochem. Commun.* **2007**, *9*, 1969–1974.
[23] Y. Zhang, X. Zhu, G. Zhang, P. Shi, A.-L. Wang, *J Mater Chem A Mater* **2021**, *9*, 5890–5914.
[24] R. Kötz, S. Stucki, D. Scherson, D. M. Kolb, *J. Electroanal. Chem. Interfacial Electrochem.* **1984**, *172*, 211–219.
[25] V. Pfeifer, T. E. Jones, J. J. Velasco Vélez, C. Massué, M. T. Greiner, R. Arrigo, D. Teschner, F. Girgsdies, M. Scherzer, J. Allan, M. Hashagen, G. Weinberg, S. Piccinin, M. Hävecker, A. Knop-Gericke, R. Schlögl, *Phys. Chem. Chem. Phys.* **2016**, *18*, 2292–2296.
[26] W. T. Hong, R. E. Welsch, Y. Shao-Horn, *J. Phys. Chem. C* **2016**, *120*, 78–86.
[27] V. Pfeifer, T. E. Jones, J. J. Velasco Vélez, R. Arrigo, S. Piccinin, M. Hävecker, A. Knop-Gericke, R. Schlögl, *Chem. Sci.* **2017**, *8*, 2143–2149.
[28] J. Ruiz Esquius, D. J. Morgan, G. Algara Siller, D. Gianolio, M. Aramini, L. Lahn, O. Kasian, S. A. Kondrat, R. Schlögl, G. J. Hutchings, R. Arrigo, S. J. Freakley, *J. Am. Chem. Soc.* **2023**, *145*, 6398–6409.
[29] C. Scherb, R. Koehn, T. Bein, *J. Mater. Chem.* **2010**, *20*, 3046–3051.
[30] A. Minguzzi, C. Locatelli, O. Lugaresi, E. Achilli, G. Cappelletti, M. Scavini, M. Coduri, P. Masala, B. Sacchi, A. Vertova, P. Ghigna, S. Rondinini, *ACS Catal.* **2015**, *5*, 5104–5115.
[31] N. Deka, T. E. Jones, L. J. Falling, L.-E. Sandoval-Diaz, T. Lunkenbein, J.-J. Velasco-Velez, T.-S. Chan, C.-H. Chuang, A. Knop-Gericke, R. V. Mom, *ACS Catal.* **2023**, *13*, 7488–7498.
[32] J. Ruiz Esquius, D. J. Morgan, I. Spanos, D. G. Hewes, S. J. Freakley, G. J. Hutchings, *ACS Appl. Energ. Mater.* **2020**, *3*, 800–809.
[33] T. Wu, S. Sun, J. Song, S. Xi, Y. Du, B. Chen, W. A. Sasangka, H. Liao, C. L. Gan, G. G. Scherer, L. Zeng, H. Wang, H. Li, A. Grimaud, Z. J. Xu, *Nat. Catal.* **2019**, *2*, 763–772.
[34] S. Zuo, Z. Wu, H. Zhang, X. W. (David) Lou, *Adv. Energy Mater.* **2022**, *12*, DOI 10.1002/aenm.202103383.
[35] A. Grimaud, O. Diaz-Morales, B. Han, W. T. Hong, Y.-L. Lee, L. Giordano, K. A. Stoerzinger, M. T. M. Koper, Y. Shao-Horn, *Nat. Chem.* **2017**, *9*, 457–465.
[36] G. Fu, X. Wen, S. Xi, Z. Chen, W. Li, J.-Y. Zhang, A. Tadich, R. Wu, D.-C. Qi, Y. Du, J. Cheng, K. H. L. Zhang, *Chem. Mater.* **2019**, *31*, 419–428.
[37] J. Y. Zhang, W. W. Li, R. L. Z. Hoye, J. L. MacManus-Driscoll, M. Budde, O. Bierwagen, L. Wang, Y. Du, M. J. Wahila, L. F. J. Piper, T.-L. Lee, H. J. Edwards, V. R. Dhanak, K. H. L. Zhang, *J. Mater. Chem. C* **2018**, *6*, 2275–2282.

ChemElectroChem

Review

doi.org/10.1002/celc.202300761

Chemistry Europe
European Chemical
Societies Publishing

[38] L. Lv, Z. Yang, K. Chen, C. Wang, Y. Xiong, *Adv. Energy Mater.* **2019**, *9*, DOI 10.1002/aenm.201803358.

[39] Y. Wu, M. Song, Y.-C. Huang, C.-L. Dong, Y. Li, Y. Lu, B. Zhou, D. Wang, J. Jia, S. Wang, Y. Wang, *J. Energy Chem.* **2022**, *74*, 140–148.

[40] Y. S. Park, J.-Y. Jeong, M. J. Jang, C.-Y. Kwon, G. H. Kim, J. Jeong, J. Lee, J. Lee, S. M. Choi, *J. Energy Chem.* **2022**, *75*, 127–134.

[41] L.-A. Stern, X. Hu, *Faraday Discuss.* **2014**, *176*, 363–379.

[42] X. Zhou, H. Dong, A.-M. Ren, *Int. J. Hydrogen Energy* **2016**, *41*, 5670–5681.

[43] K. L. Nardi, N. Yang, C. F. Dickens, A. L. Strickler, S. F. Bent, *Adv. Energy Mater.* **2015**, *5*, DOI 10.1002/aenm.201500412.

[44] W. D. Chemelewski, H.-C. Lee, J.-F. Lin, A. J. Bard, C. B. Mullins, *J. Am. Chem. Soc.* **2014**, *136*, 2843–2850.

[45] P. F. Liu, S. Yang, L. R. Zheng, B. Zhang, H. G. Yang, *J. Mater. Chem. A* **2016**, *4*, 9578–9584.

[46] A. Singh, S. L. Y. Chang, R. K. Hocking, U. Bach, L. Spiccia, *Energy Environ. Sci.* **2013**, *6*, 579–586.

[47] Y.-F. Li, A. Selloni, *ACS Catal.* **2014**, *4*, 1148–1153.

[48] I. M. Sadiek, A. M. Mohammad, M. E. El-Shakre, M. S. El-Deab, *Int. J. Hydrogen Energy* **2012**, *37*, 68–77.

[49] S. Klaus, Y. Cai, M. W. Louie, L. Trotochaud, A. T. Bell, *J. Phys. Chem. C* **2015**, *119*, 7243–7254.

[50] M. S. Burke, L. J. Enman, A. S. Batchellor, S. Zou, S. W. Boettcher, *Chem. Mater.* **2015**, *27*, 7549–7558.

[51] L. Trotochaud, S. L. Young, J. K. Ranney, S. W. Boettcher, *J. Am. Chem. Soc.* **2014**, *136*, 6744–6753.

[52] L. Trotochaud, J. K. Ranney, K. N. Williams, S. W. Boettcher, *J. Am. Chem. Soc.* **2012**, *134*, 17253–17261.

[53] M. S. Burke, M. G. Kast, L. Trotochaud, A. M. Smith, S. W. Boettcher, *J. Am. Chem. Soc.* **2015**, *137*, 3638–3648.

[54] X. Lu, H. Xue, H. Gong, M. Bai, D. Tang, R. Ma, T. Sasaki, *Nano-Micro Lett.* **2020**, *12*, 86.

[55] X. Wan, Y. Song, H. Zhou, M. Shao, *Energy Material Advances* **2022**, *2022*, DOI 10.34133/2022/9842610.

[56] D. Alves, P. R. Kasturi, G. Collins, T. N. Barwa, S. Ramaraj, R. Karthik, C. B. Breslin, *Mater Adv* **2023**, *4*, 6478–6497.

[57] D. Monga, S. Sharma, N. P. Shetti, S. Basu, K. R. Reddy, T. M. Aminabhavi, *Mater. Today Chem.* **2021**, *19*, 100399.

[58] X. Peng, Y. Yan, X. Jin, C. Huang, W. Jin, B. Gao, P. K. Chu, *Nano Energy* **2020**, *78*, 105234.

[59] T. Wulandari, D. Fawcett, S. B. Majumder, G. E. J. Poinern, *Battery Energy* **2023**, *2*, DOI 10.1002/bte2.20230030.

[60] M. Holzapfel, A. Würsig, W. Scheifele, J. Vetter, P. Novák, *J. Power Sources* **2007**, *174*, 1156–1160.

[61] K. Mizushima, P. C. Jones, P. J. Wiseman, J. B. Goodenough, *Mater. Res. Bull.* **1980**, *15*, 783–789.

[62] Y. Kim, E. Choi, S. Kim, H. R. Byon, *Chem. Sci.* **2023**, *14*, 10644–10663.

[63] S. W. Lee, C. Carlton, M. Risch, Y. Surendranath, S. Chen, S. Furutsuki, A. Yamada, D. G. Nocera, Y. Shao-Horn, *J. Am. Chem. Soc.* **2012**, *134*, 16959–16962.

[64] Z. Lu, H. Wang, D. Kong, K. Yan, P.-C. Hsu, G. Zheng, H. Yao, Z. Liang, X. Sun, Y. Cui, *Nat. Commun.* **2014**, *5*, 4345.

[65] Y. Takahashi, N. Kijima, K. Tokiwa, T. Watanabe, J. Akimoto, *J. Phys. Condens. Matter* **2007**, *19*, 436202.

[66] H. Wang, L. Wang, Y. Jia, X. Li, H. Yang, X. Zhu, Q. Bu, Q. Liu, *Inorg. Chem.* **2023**, *62*, 11256–11264.

[67] Y. Hao, J. Li, X. Cao, L. Meng, J. Wu, X. Yang, Y. Li, Z. Liu, M. Gong, *ACS Catal.* **2023**, *13*, 2916–2927.

[68] E. Bianchetti, D. Perilli, C. Di Valentin, *ACS Catal.* **2023**, *13*, 4811–4823.

[69] J. Kang, X. Yang, Q. Hu, Z. Cai, L.-M. Liu, L. Guo, *Chem. Rev.* **2023**, *123*, 8859–8941.

[70] D. Rathore, A. Banerjee, S. Pande, *ACS Appl. Nano Mater.* **2022**, *5*, 2664–2677.

[71] L. Wang, V. A. Saveleva, M. J. Eslamibidgoli, D. Antipin, C. Bouillet, I. Biswas, A. S. Gago, S. S. Hosseiny, P. Gazdzicki, M. H. Eikerling, E. R. Savinova, K. A. Friedrich, *ACS Appl. Energ. Mater.* **2022**, *5*, 2221–2230.

[72] A. Sakamaki, M. Yoshida-Hirahara, H. Ogihara, H. Kurokawa, *Langmuir* **2022**, *38*, 5525–5531.

[73] A. Venugopal, L. H. T. Egberts, J. Meeprasert, E. A. Pidko, B. Dam, T. Burdyny, V. Sinha, W. A. Smith, *ACS Energy Lett.* **2022**, *7*, 1586–1593.

[74] S.-J. Guan, P. Zhang, S.-J. Ji, Y. Cao, N.-T. Suen, *Inorg. Chem.* **2022**, *61*, 12772–12780.

[75] Y. Zhu, W. Zhou, Y. Chen, J. Yu, M. Liu, Z. Shao, *Adv. Mater.* **2015**, *27*, 7150–7155.

[76] F. Liang, Y. Yu, W. Zhou, X. Xu, Z. Zhu, *J. Mater. Chem. A* **2015**, *3*, 634–640.

[77] X. Liu, M. Park, M. G. Kim, S. Gupta, G. Wu, J. Cho, *Angew. Chem. Int. Ed.* **2015**, *54*, 9654–9658.

[78] R. Liu, F. Liang, W. Zhou, Y. Yang, Z. Zhu, *Nano Energy* **2015**, *12*, 115–122.

[79] H. Ji, G. Sahasrabudhe, M. K. Vallon, J. Schwartz, A. B. Bocarsly, R. J. Cava, *Mater. Res. Bull.* **2017**, *95*, 285–291.

[80] R. E. Schaak, T. Klimczuk, M. L. Foo, R. J. Cava, *Nature* **2003**, *424*, 527–529.

[81] G. Gardner, J. Al-Sharab, N. Danilovic, Y. B. Go, K. Ayers, M. Greenblatt, G. Charles Dismukes, *Energy Environ. Sci.* **2016**, *9*, 184–192.

[82] B. Weng, F. Xu, C. Wang, W. Meng, C. R. Grice, Y. Yan, *Energy Environ. Sci.* **2017**, *10*, 121–128.

[83] V. Soni, R. Mondal, A. N. Singh, P. Singh, A. Gupta, *ACS Appl. Energ. Mater.* **2023**, *6*, 1308–1320.

[84] A. Gupta, W. D. Chemelewski, C. Buddie Mullins, J. B. Goodenough, *Adv. Mater.* **2015**, *27*, 6063–6067.

[85] V. Augustyn, A. Manthiram, *J. Phys. Chem. Lett.* **2015**, *6*, 3787–3791.

[86] X. Ren, C. Wei, Y. Sun, X. Liu, F. Meng, X. Meng, S. Sun, S. Xi, Y. Du, Z. Bi, G. Shang, A. C. Fisher, L. Gu, Z. J. Xu, *Adv. Mater.* **2020**, *32*, 2001292.

[87] J. Gao, C. Q. Xu, S. F. Hung, W. Liu, W. Cai, Z. Zeng, C. Jia, H. M. Chen, H. Xiao, J. Li, Y. Huang, B. Liu, *J. Am. Chem. Soc.* **2019**, *141*, 3014–3023.

[88] M. Sathiya, G. Rousse, K. Ramesha, C. P. Laisa, H. Vezin, M. T. Sougrati, M.-L. Doublet, D. Foix, D. Gonbeau, W. Walker, A. S. Prakash, M. Ben Hassine, L. Dupont, J.-M. Tarascon, *Nat. Mater.* **2013**, *12*, 827–835.

[89] M. Sathiya, A. M. Abakumov, D. Foix, G. Rousse, K. Ramesha, M. Saubanère, M. L. Doublet, H. Vezin, C. P. Laisa, A. S. Prakash, D. Gonbeau, G. VanTendeloo, J.-M. Tarascon, *Nat. Mater.* **2015**, *14*, 230–238.

[90] M. J. O'Malley, H. Verweij, P. M. Woodward, *J. Solid State Chem.* **2008**, *181*, 1803–1809.

[91] S. K. Choi, R. Coldea, A. N. Kolmogorov, T. Lancaster, I. I. Mazin, S. J. Blundell, P. G. Radaelli, Y. Singh, P. Gegenwart, K. R. Choi, S.-W. Cheong, P. J. Baker, C. Stock, J. Taylor, *Phys. Rev. Lett.* **2012**, *108*, 127204.

[92] H. Kobayashi, M. Tabuchi, M. Shikano, H. Kageyama, R. Kanno, *J. Mater. Chem.* **2003**, *13*, 957–962.

[93] K. M. Mogare, K. Friese, W. Klein, M. Jansen, *Z. Anorg. Allg. Chem.* **2004**, *630*, 547–552.

[94] C. Yang, G. Rousse, K. Louise Svane, P. E. Pearce, A. M. Abakumov, M. Deschamps, G. Cibin, A. V. Chadwick, D. A. Dalla Corte, H. Anton Hansen, T. Vegge, J.-M. Tarascon, A. Grimaud, *Nat. Commun.* **2020**, *11*, 1378.

[95] L. Li, F. C. Castro, J. S. Park, H. Li, E. Lee, T. D. Boyko, J. W. Freeland, Z. Yao, T. T. Fister, J. Vinson, E. L. Shirley, C. Wolverton, J. Cabana, V. P. Dravid, M. M. Thackeray, M. K. Y. Chan, *Chem. Mater.* **2019**, *31*, 4341–4352.

[96] J. Hong, W. E. Gent, P. Xiao, K. Lim, D.-H. Seo, J. Wu, P. M. Csernica, C. J. Takacs, D. Nordlund, C.-J. Sun, K. H. Stone, D. Passarello, W. Yang, D. Prendergast, G. Ceder, M. F. Toney, W. C. Chueh, *Nat. Mater.* **2019**, *18*, 256–265.

[97] A. Biffin, R. D. Johnson, S. Choi, F. Freund, S. Manni, A. Bombardi, P. Manuel, P. Gegenwart, R. Coldea, *Phys. Rev. B* **2014**, *90*, 205116.

[98] C. Yang, G. Rousse, K. Louise Svane, P. E. Pearce, A. M. Abakumov, M. Deschamps, G. Cibin, A. V. Chadwick, D. A. Dalla Corte, H. Anton Hansen, T. Vegge, J.-M. Tarascon, A. Grimaud, *Nat. Commun.* **2020**, *11*, 1378.

[99] M.-S. Park, Y.-G. Lim, J.-W. Park, J.-S. Kim, J.-W. Lee, J. H. Kim, S. X. Dou, Y.-J. Kim, *J. Phys. Chem. C* **2013**, *117*, 11471–11478.

[100] P. E. Pearce, C. Yang, A. Iadecola, J. Rodriguez-Carvajal, G. Rousse, R. Dedryvère, A. M. Abakumov, D. Giaume, M. Deschamps, J. M. Tarascon, A. Grimaud, *Chem. Mater.* **2019**, *31*, 5845–5855.

[101] L. C. Seitz, C. F. Dickens, K. Nishio, Y. Hikita, J. Montoya, A. Doyle, C. Kirk, A. Vojvodic, H. Y. Hwang, J. K. Norskov, T. F. Jaramillo, *Science* **2016**, *353*, 1011–1014.

[102] G. Wan, J. W. Freeland, J. Kloppenburg, G. Petretto, J. N. Nelson, D.-Y. Kuo, C.-J. Sun, J. Wen, J. T. Diulus, G. S. Herman, Y. Dong, R. Kou, J. Sun, S. Chen, K. M. Shen, D. G. Schlom, G.-M. Rignanese, G. Hautier, D. D. Fong, Z. Feng, H. Zhou, J. Suntivich, *Sci. Adv.* **2021**, *7*, eabc7323.

[103] H. G. Sanchez Casalongue, M. L. Ng, S. Kaya, D. Friebel, H. Ogasawara, A. Nilsson, *Angew. Chem. Int. Ed.* **2014**, *53*, 7169–7172.

ChemElectroChem

Review
doi.org/10.1002/celc.202300761

**Chemistry Europe**
European Chemical
Societies Publishing

[104] V. Pfeifer, T. E. Jones, S. Wrabetz, C. Massué, J. J. Velasco Vélez, R. Arrigo, M. Scherzer, S. Piccinin, M. Hävecker, A. Knop-Gericke, R. Schlögl, *Chem. Sci.* **2016**, *7*, 6791–6795.

[105] W. Sun, Y. Song, X.-Q. Gong, L. Cao, J. Yang, *ACS Appl. Mater. Interfaces* **2016**, *8*, 820–826.

[106] N. Bestaoui, P. Deniard, R. Brec, *J. Solid State Chem.* **1995**, *118*, 372–377.

[107] L. Zhu, C. Ma, L. Cao, J. Yang, *ACS Appl. Energ. Mater.* **2023**, *6*, 4757–4765.

[108] B. Weng, F. Xu, C. Wang, W. Meng, C. R. Grice, Y. Yan, *Energy Environ. Sci.* **2017**, *10*, 121–128.

[109] V. Soni, R. Mondal, A. N. Singh, P. Singh, A. Gupta, *ACS Appl. Energ. Mater.* **2023**, *6*, 1308–1320.

REVIEW

Layered metal oxides containing intercalated alkali metals are promising catalysts for the oxygen evolution reaction (OER) which are needed for efficient water electrolysis. Here we review recent developments of such alkali metal-layered materials, focusing on their structure, nature of intercalated species, and the role of metal dopants on catalytic performance in terms of activity and stability.
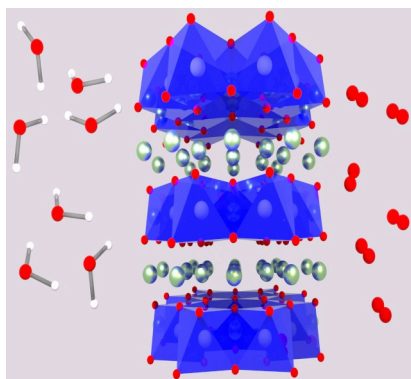
M. Falsaperna*, R. Arrigo, F. Marken, S. J. Freakley*

Alkali Containing Layered Metal Oxides as Catalysts for the Oxygen Evolution Reaction